A Comprehensive Study of Buoyant Rosette Jets using Laboratory Experiments, CFD, and Machine Learning

Shuyi Jia

Thesis submitted to the University of Ottawa
in partial Fulfillment of the requirements for the
Master of Applied Science in Civil Engineering

Department of Civil Engineering
Academic Supervisors: Prof. Hossein Bonakdari, Prof. Abdolmajid Mohammadian
University of Ottawa

Abstract

Rosette diffusers are increasingly used in modern outfall designs due to their unique structure and efficient initial dilution performance. However, the complex mixing behavior of the resulting buoyant jets poses a challenge for accurate modeling, requiring more advanced mixing methods. This study integrates laboratory laser-induced fluorescence (LIF) experiments, computational fluid dynamics (CFD) simulations, and machine learning (ML) modeling to conduct a comprehensive analysis of buoyant rosette multiport jets. The main goal is to improve the accuracy, efficiency, and interpretability of trajectory and normalized concentration field predictions in wastewater discharge systems.

Experiments were conducted using LIF techniques to obtain high-resolution scalar concentration fields, and visual jet trajectory data under different operating conditions were obtained. These experimental results can be used as a benchmark dataset for validating CFD simulations and training ML models. CFD simulations were performed using a modified version of the OpenFOAM benchmark solver pimpleFoam, which incorporates temperature-driven buoyancy effects while ignoring salinity transport to reduce computational costs. The prediction performance of three RANS turbulence models - standard k-ε, RNG k-ε, and SST k-ω - was evaluated for two different Fr number cases (high Fr number 5.81 and low Fr number 2.23). The RNG k-ε model performs well in predicting centerline trajectories and concentration fields under momentum-dominated conditions, thanks to its enhanced formulation, including an improved turbulent transport model and an additional ε equation term. Importantly, the model achieves higher accuracy than the standard k-ε model without significantly increasing computational time.

To address the limitations of CFD and experimental coverage near the nozzle region, three machine learning models—extreme learning machine (ELM), adaptive neuro-fuzzy inference system (ANFIS), and multivariate adaptive regression splines (MARS)—are trained on 870 data points from 34 different Fr number cases obtained experimentally. Input features included Fr number, x/D, and y/D, while the target variable was normalized concentration. ANFIS outperforms the other models on the test dataset with an R^2 of 0.9088 and an RMSE of 0.0551. ELM exhibits high accuracy and fast training speed, while MARS provides an interpretable piecewise linear representation but has limited generalization capabilities. The results show that combining LIF experiments with ML algorithms can effectively reduce the reliance on resource-intensive CFD while maintaining prediction accuracy.

This comprehensive hybrid experiment-CFD and experiment-ML integrated framework provides a reliable solution for rosette jet dynamics modeling, diffuser design optimization, and environmental impact assessment under different hydraulic conditions. Future work suggestions include improving the experimental density control, integrating optimization algorithms with ML models, and extending the application to real-time scenarios.

Acknoledgements

During my master's studies, I received help and encouragement from many people, and I would like to express my deep gratitude to them.

Firstly, I would like to thank my supervisors, Prof. Abdolmajid Mohammadian and Prof. Hossein Bonakdari, for their guidance on my research project. Prof. Abdolmajid Mohammadian was my mentor in learning OpenFOAM, and throughout my studies, he guided me on simulation runs, experimental procedures, and even the details of my thesis. His meticulous guidance has been immensely beneficial to me. Prof. Hossein Bonakdari provided me with tremendous assistance and support in the field of machine learning. Under his guidance, I gained an understanding of the operation and performance of various machine learning models, which allowed me to make progress in this previously unexplored area. Additionally, his revisions and polishing of my thesis helped me improve my writing skills. Without the academic guidance and constant encouragement of my two advisors, which boosted my confidence, I would not have been able to complete my master's degree in one year. I would like to express my deepest gratitude to them. In my future academic career, I will continue to strive hard and live up to their guidance.

Secondly, I would like to thank my laboratory colleagues Danial Goodarzi, Sina Tahmooresi, and Mark Lapointe. Danial Goodarzi patiently taught me the principles of LIF experiments and personally guided me through the entire experimental process. Sina Tahmooresi taught me the procedures for conducting PIV experiments using new equipment. Mark Lapointe helped me understand and resolve laboratory safety precautions and facility issues. Experiments are a vital part of my research, and I am very grateful to them for their tremendous help with my experiments. In addition, I would like to thank Dr. Xiaohui Yan and Dr. Xinyun Wang, whose enthusiastic help solved many of my simulation problems.

Next, I would like to thank Lingkun Meng for his consistent patience and assistance in my studies, both in experiments and simulations. I would also like to thank my friend Mengqian Zhang, for her constant companionship and encouragement, which has made me more confident and courageous in pursuing excellence.

Finally, I would like to thank my parents, Junhu Jia and Wenli Niu, for their continuous financial support and emotional encouragement. It is because of them that I have had the opportunity and courage to pursue further studies. They are the pillars of strength in my life.

Table of Contents

List of Figures

List of Tables

List of Symbols

k	Turbulent kinetic energy	m^2 / s^2
ε	Dissipation rate	m^2 / s^3
ω	Specific dissipation rate	s^{-1}
Fr	Froude number	
D	Riser diameter	m
d	Nozzle diameter	m
Fr_d	Densimetric Froude number	
d	Nozzle diameter	m
U	Jet velocity	m / s
g'	Reduced gravity	m / s^2
$\rho_{effluent}$	Effluents density	kg / m^3
$\rho_{ambient}$	Ambient water density	kg / m^3
λ_{ex}	Excitation wavelength	nm
Re	Reynolds number	
$\Delta\rho$	Density difference	kg / m^3
ρ_j	Jet density	kg / m^3
ρ_a	Ambient water density	kg / m^3
h	Depth	m
k	Ratio of jet velocity to ambient water velocity	
u_0	Jet velocity	m / s
u_a	Ambient water velocity	m / s
T_j	Jet temperature	$°C$
T_a	Ambient water temperature	$°C$
U_j	Jet velocity	m / s
g	Gravity acceleration	m / s^2
u, v, w	Velocity in the x, y, z direction, respectively	m / s
t	Time	s

P	Fluid pressure	Pa
ρ	Fluid density	kg / m^3
ρ_0	Reference fluid density	kg / m^3
υ_{eff}	Effective kinematic viscosity	m^2 / s
υ	Molecular kinematic viscosity	m^2 / s
υ_t	Turbulent kinematic viscosity	m^2 / s
ρ_t	Density of water that varies with the temperature	kg / m^3
T	Temperature of water	$°C$
S	Salinity	
A	Temperature-dependent coefficient for the linear salinity term	kg / m^3
B	Coefficient for the nonlinear salinity term	kg / m^3
C	Coefficient for the salinity squared term	kg / m^3
G_k	Generation of turbulent kinetic energy due to mean velocity gradients	m^2 / s^3
Dk_{eff}	Effective diffusivity for k	m^2 / s
$D\varepsilon_{eff}$	Effective diffusivity for ε	m^2 / s
σ_ε	Turbulent Prandtl number for ε	
$C_{1\varepsilon},\ C_{2\varepsilon},\ C_\mu$	Constants that have been derived experimentally	
$u_i^{'},\ u_j^{'},\ S_{ij}$	Fluctuating parts of velocity and strain-rate tensor respectively	$m/s,\ m/s,\ s^{-1}$
R	Renormalization term	m^2 / s^3
$C_\mu,\ C_{1\varepsilon},\ C_{2\varepsilon},\ \sigma_k,\ \sigma_\varepsilon,\ \eta_0,\ \beta$	Constants	
$A_1,\ \alpha_{k1},\ \alpha_{k2},\ \alpha_{\omega 1},\ \alpha_{\omega 2},\ \beta_1,\ \beta_2,\ \beta^*,\ \gamma_1,\ \gamma_1.$	Constants	
C	Concentration	
$\widehat{C}$	Normalized concentration	
$x,\ y,\ z$	Coordinate	

List of Acronyms

LIF	Laser Induced Fluorescence
CFD	Computational Fluid Dynamic
ML	Mahcine Learning
OpenFOAM	Open Field Operation and Manipulation
RANS	Reynolds-Averaged Navier-Stokes
RNG	Renormalization Group
SST	Shear Stress Transport
ELM	Extreme Learning Machine
ANFIS	Adaptive Neuro Fuzzy Inference System
MARS	Multivariate Adaptive Regression Splines
RMSE	Root Mean Squared Error
TKE	Turbulent Kinetic Energy
DES	Detached Eddy Simulation
LES	Large Eddy Simulation
HPC	High-Performance Computing
PIV	Particle Image Velocimetry
MIR	Merging-In-a-Riser
MBR	Merging-between-Risers
PLIF	Planar Laser Induced Fluorescence
NRMSE	Normalized Root Mean Square Error
SIMPLE	Semi-Implicit Method for Pressure-Linked Equations
PISO	Pressure-Implicit with Splitting of Operators
GA	Genetic Algorithms
PSO	Particle Swarm Optimization
FA	Firefly Algorithm
ROC	Receiver Operating Characteristic
AUC	Area Under the Curve
AI	Artificial Intelligence
MGGP	Multi-Gene Genetic Programming
CNN	Convolutional Neural Network

MAE	Mean Absolute Error
BF	Basis Functions

Chapter I Introduction

1.1 Introduction and motivation

Fluid jets are fundamental phenomena in environmental engineering, industrial processes, and natural systems, and play a key role in applications such as wastewater discharge, combustion, and thermal management. The mixing process of wastewater jets is very sensitive to the configuration of the diffuser. The use of multiport diffusers is becoming common practice. Depending on how the ports are configured, multiport diffuser users can be divided into different types, such as unidirectional, T-shaped, and rosette-shaped. Among the various multiple ports diffuser configurations, the rosette-type multiport diffuser has been widely used in submarine wastewater discharge systems in densely populated coastal areas. The rosette-type multiport diffuser achieves dispersed discharge of partially treated wastewater through circumferentially distributed nozzles (Figure 1). The spatial constraints and environmental regulations in these areas require compact and efficient discharge port designs. When multiport buoyant jets are discharged in close proximity, their interactions (controlled by momentum exchange, buoyancy effects, and turbulence) determine their merging behavior, which directly affects the mixing efficiency and environmental compliance, greatly increasing the difficulty of dilution pattern prediction and diffuser optimization design and posing a severe challenge to the goal of minimizing ecological risks (Yan et al., 2021; Seo & Yeo, 2002).

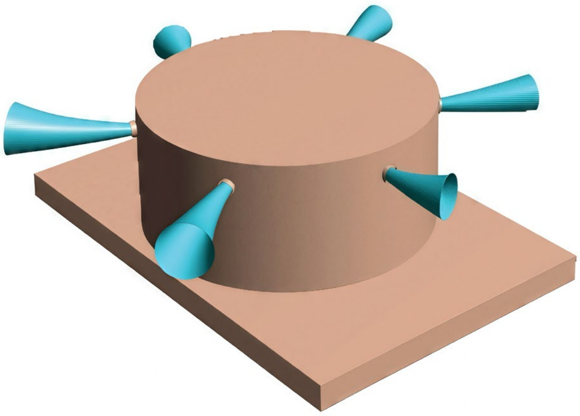

Fig. 1.1 Rosette-type diffuser with 6 nozzles (Lai et al., 2011).

1.1.1 Rosette jet classification

Rosette-type jets refer to buoyant discharges emitted from multiport diffusers with nozzles arranged circumferentially, forming a radial pattern akin to a flower rosette. These configurations are widely adopted in submarine wastewater outfalls to enhance mixing efficiency through controlled interactions between adjacent jets (Seo et al., 2004). The classification of rosette jets is pivotal for understanding their hydrodynamic behavior and optimizing diffuser designs. Key classification criteria include:

1. Number of nozzles

The number of nozzles in multiport diffusers is usually configured from 2 to 8, among which the 6-nozzle design is widely adopted for its optimal balance between compactness and mixing performance (Tian & Roberts, 2011). As shown in Figure 2, the 6-nozzle rosette diffuser discharges wastewater. Studies have shown that optimizing the symmetrical geometric layout (uniform distribution of nozzles around the circumference) and the Froude number (Fr) can effectively suppress premature jet merging and increase the near-field dilution rate (Yan et al., 2021).

Spacing and Orientation: Nozzles are usually evenly spaced along the circumference of the diffuser. Smaller port-to-port distances (D/d) enhance jet interactions and accelerate merging, while larger spacing maintains the individuality of the jets (Seo et al., 2004).

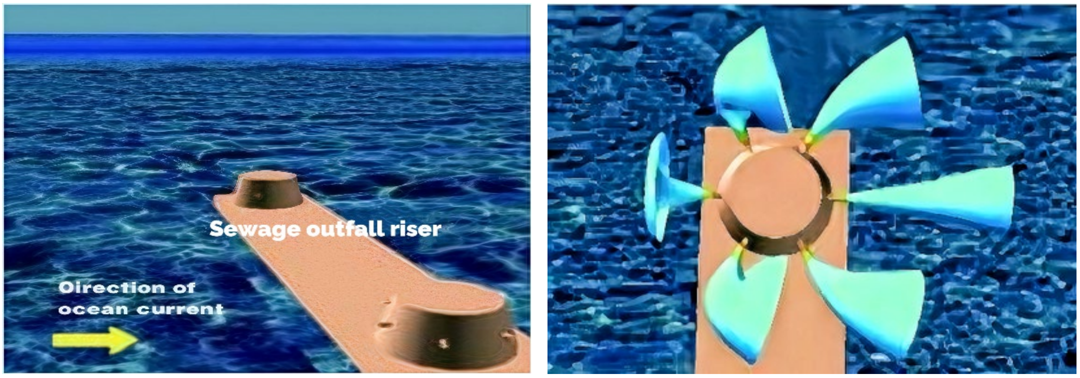

Fig. 2 a) Sewage outfall diffuser b) Rosette-shaped buoyant jets (overhead view): The effluents are being discharged in six jets (Cheung et al., 2000).

2. Flow characteristics

Buoyancy-Dominant vs. Momentum-Dominant: Jets are classified based on the densimetric Froude number ($Fr_d = U / \sqrt{g'd}$), where g' is reduced gravity. Low Fr_d (Fr_d<1) indicates buoyancy-driven flows with pronounced vertical rise, whereas high Fr_d (Fr_d>1) signifies momentum-dominated horizontal spreading (Yan et al., 2021).

Stratification Effects: In stratified environments, jets may exhibit distinct merging patterns depending on ambient density gradients (Lai et al., 2011).

3. Jet type based on density

The relative density of discharged effluent further categorizes rosette jets compared to the receiving water:

Rosette Buoyant Jets: Effluents are less dense than the ambient water ($\rho_{effluent} < \rho_{ambient}$), causing jets to rise vertically due to positive buoyancy. The upward motion promotes lateral spreading as they interact with the surrounding fluid, enhancing dilution (Seo & Yeo, 2002). This behavior is common in wastewater discharges where effluent temperatures or salinity levels differ from the receiving water.

Rosette Dense Jets: Effluents are denser than the ambient water ($\rho_{effluent} > \rho_{ambient}$), leading to downward sinking. These jets disperse near the seabed, posing risks of localized contamination and requiring careful design to avoid sediment resuspension (Roberts et al., 2010).

1.1.2 Focus of this study

This research specifically investigates rosette buoyant jets, which are prevalent in municipal and industrial wastewater outfalls. Their upward trajectory and lateral spreading mechanisms are critical for achieving regulatory dilution standards while minimizing environmental impact. By contrast, dense jets involve distinct challenges (e.g., stratification stability and benthic impacts) that fall outside the scope of this work.

1.2 Research objectives and significance

This study integrates experimental, computational, and machine learning (ML) approaches to enhance understanding prediction and optimization of buoyant rosette jets in wastewater discharge systems, which is significant in addressing key environmental engineering challenges related to pollutant dispersion and water quality near outfalls. The findings will contribute to more sustainable and efficient design of wastewater discharge systems in both urban and coastal environments. The study aims to:

1. Experimentally characterize the jet behavior of buoyant rosette jets using Laser-Induced Fluorescence (LIF) techniques under different running parameters, thereby generating high-quality benchmark datasets for validation purposes.
2. The buoyant rosette jet behavior is numerically simulated using various Reynolds-Averaged Navier–Stokes (RANS) turbulence models within the OpenFOAM framework to evaluate their accuracy in capturing complex jet interactions and associated flow structures.
3. Develop and train machine learning models—including Extreme Learning Machine (ELM), Adaptive Neuro-Fuzzy Inference System (ANFIS), and Multivariate Adaptive Regression Splines (MARS) on hybrid CFD-experimental datasets to predict key jet characteristics.

The significance of this study lies in bridging gaps between costly experiments, computationally intensive simulations, and real-world applicability in wastewater discharge system design. By integrating LIF-based experimentation, high-fidelity CFD modeling, and advanced ML techniques, this work:

1. Provide a cost-effective experimental-CFD hybrid framework to establish a cost-effective and reliable method for optimizing diffuser design, especially by evaluating the impact of key parameters such as Froude number on jet performance.
2. Demonstrate the ability of the Adaptive-network-based fuzzy inference system (ANFIS) model to outperform traditional machine learning algorithms in predicting normalized concentrations of buoyant jets, providing a novel and efficient tool for accurate flow field prediction under different operating conditions.
3. Promote the development of scalable and transferable modeling solutions for various discharge scenarios, including riverine, estuarine and coastal environments, thereby supporting data-driven, sustainable design and management of wastewater outfalls and protecting sensitive aquatic ecosystems.

1.3 Novelty and contributions of research

This study introduces novel methodologies and delivers impactful contributions to the fields of environmental fluid mechanics and computational modeling:

1. Hybrid Experimental-CFD and Experimental-ML Framework

- Novelty: This study proposes a dual-integrated framework that combines laboratory-scale Laser-Induced Fluorescence (LIF) experiments with both computational fluid dynamics (CFD) simulations and machine learning (ML) modeling. By fusing experimental–CFD and experimental–ML approaches, the framework addresses the limitations of each standalone method—specifically, the difficulty of capturing detailed flow structures near the nozzle in experiments and the high computational cost of CFD.
- Contribution: The proposed framework enables accurate and efficient prediction of jet behavior and concentration fields in buoyant rosette-type discharges. Validated against experimental data, it offers a data-driven modeling strategy that supports improved diffuser design and environmental impact assessment in coastal wastewater discharge applications.

2. Methodological Advancements in CFD and ML

- Novelty: Demonstrated that the RNG k-ε model outperforms the standard k-ε and SST k-ω models in capturing the turbulent characteristics of rosette-type jets, as validated against experimental data. In parallel, the ANFIS model showed the highest predictive accuracy among the tested machine learning algorithms (ANFIS, ELM, MARS) for modeling normalized concentration fields.
- Contribution: Established a systematic methodology for selecting both the most suitable turbulence model and the most effective machine learning algorithm for simulating multiport buoyant jets. This dual-guidance framework reduces trial-and-error in environmental engineering design and supports more efficient development of wastewater discharge systems.

1.4 Thesis outline

This thesis is structured to address the research objectives and contributions systematically. The outline is as follows:

- Chapter 1: Introduction - Outlines the background, motivation, research objectives, and significance of the study, setting the stage for the subsequent research.
- Chapter 2: Experimental and CFD study of buoyant rosette jet - Reviews rosette jet dynamics, analyzes turbulence models, identifies experimental-CFD framework gaps.
- Chapter 3: Application of machine learning in simulation of buoyant rosette jet - Combines LIF experiments and ML, achieves faster simulations with validated accuracy.
- Chapter 4: Conclusions and recommendations - Synthesizes the main findings of the study and outlines recommendations for future research and practical applications.

This study presents an efficient integrated approach to predict the behavior of buoyant rosettes multiport jet by combining experimental data with CFD simulations and machine learning. This approach improves modeling accuracy while providing practical value for future diffuser design and environmental applications.

Chapter II Experimental and CFD Study of Buoyant Rosette Jet

2.1 Introduction and literature review

2.1.1 Introduction

The hydrodynamic behavior of buoyant jets discharged through multiport configurations, such as rosette-type diffusers, critically governs their efficacy in pollutant dispersion and their ultimate environmental impacts on aquatic ecosystems. Numerical models alongside theoretical frameworks (Jirka, 1977; Fischer, 1979) have delivered basic understandings about jet dynamics yet experimental verification continues to be essential for analyzing the complex dynamics of turbulent buoyant jets especially in stationary water.

The mixing of rosette jet group discharge with the ambient flow involves the complicated interaction of coflowing, oblique-flowing, crossflowing, and counterflowing jets. Because of the complexity of the discharge configuration, ocean outfall design has typically resorted to comprehensive physical model experiments (Lai et al., 2011).

Experimental studies provide a valuable reference for understanding the flow characteristics of buoyant rose-shaped multi-port jets. Although physical experiments have shown good results in revealing local turbulent structures and verifying theoretical models, there are still certain limitations in capturing the overall spatial and temporal variation of three-dimensional flow fields, especially under conditions of high Reynolds numbers or large scales. At this stage, computational fluid dynamics (CFD) technology can be an important supplementary means to effectively bridge the gap between laboratory-controlled conditions and actual engineering applications (Saeidi Hosseini et al., 2022).

Compared with physical experiments, which are usually limited by laboratory limitations such as camera field of view, fixed position of laser sheet, and zoom requirements, computational fluid dynamics (CFD) can conduct more flexible and systematic studies. It can easily change key design variables (such as nozzle orientation, velocity ratio and diffuser geometry) and perform parametric analysis. It can also provide detailed quantitative analysis of performance indicators such as turbulent kinetic energy (TKE) dissipation and dilution efficiency at different spatial and temporal scales (Khuntia et al., 2023).

Recent advancements in turbulence modeling (e.g., detached eddy simulation, DES; large eddy simulation, LES) and high-performance computing (HPC) have further enhanced the predictive accuracy of CFD for buoyant jet systems (Jamshed, 2015; Elmisaoui et al., 2024). In addition, computational fluid dynamics (CFD) can analyze certain physical mechanisms separately through controlled numerical experiments, such as the difference between buoyancy-dominated and momentum-dominated motions, which is difficult to do in physical experiments because multiple forces in reality usually exist simultaneously and are difficult to separate.

2.1.2 Literature review

Numerous studies have investigated the behavior of buoyant jets discharged from rosette-type multiport diffusers through both laboratory experiments and numerical simulations. The mixing characteristics of such systems are governed by complex interactions between adjacent jets, diffuser geometry, and ambient conditions. To examine these phenomena, researchers have employed physical modeling techniques such as hydraulic flume experiments, particle image velocimetry (PIV), and laser-induced fluorescence (LIF), alongside computational fluid dynamics (CFD) simulations. Common CFD platforms—such as OpenFOAM, ANSYS Fluent, and COMSOL Multiphysics—are widely used to simulate jet flows across diverse environmental and geometric scenarios.

Among various jet configurations, buoyant rosette jets—consisting of multiple horizontally oriented jets arranged circumferentially around a central riser—have attracted significant attention due to their strong inter-jet interactions and complex merging behavior. Unlike single or linear multiport jets, rosette jets generate highly three-dimensional flow fields in which mutual entrainment and geometric confinement lead to inward deflection and suppressed lateral spreading. This behavior, partly attributable to the Coanda effect, results from low-pressure zones near the centerline that draw the jets inward, accelerating their merging process (Saeidi Hosseini et al., 2022; Yan et al., 2019). As a result, rosette jets often demonstrate reduced dilution efficiency compared to spatially separated configurations, highlighting the limitations of conventional line-plume models and emphasizing the need for specialized studies on rosette-type discharges.

A number of laboratory investigations have focused on understanding the mixing behavior of buoyant rosette-type jets under various discharge and ambient conditions. Isaacson et al.

(1983) conducted one of the earliest systematic physical model studies on multiport risers, observing that clustering discharge ports had little effect on near-field dilution if total discharge per unit riser length was conserved. Roberts and Snyder (1993a, 1993b), as part of the Boston Harbor outfall study, found that increasing the number of ports led to premature jet merging and lower dilution, underscoring the need for careful optimization of diffuser design. Tate (2002) developed a general Lagrangian model and validated it with experiments, demonstrating that environmental factors such as stratification could significantly affect jet rise height and dilution behavior.

Further experiments by Seo et al. (2004) introduced the concepts of merging-in-a-riser (MIR) and merging-between-risers (MBR) through flume studies in stagnant shallow water. Their results showed that increasing the number of merging jets reduced surface dilution and that merging height decreased with Froude number. Kwon and Seo (2005) employed PIV-based hydraulic experiments to investigate horizontal buoyant jets discharged from a rosette-type riser with four ports. Their study confirmed that under-pressure within the jet array induced ambient flows toward the center, resulting in inward deflection of the jet trajectories. The bending behavior was found to be strongly influenced by inter-jet entrainment and merging effects. The degree of trajectory bending increased with the densimetric Froude number up to a certain threshold, beyond which it gradually diminished as jet momentum dominated. These findings underscore the importance of accounting for pressure-induced ambient flow and Froude number–dependent behavior when modeling mixing and dilution in rosette-type diffuser systems. Lai et al. (2011) extended these findings to crossflow conditions using LIF to visualize scalar fields. Despite weakened jet-to-jet interaction under crossflow, their results still showed significant plume overlap and merging effects, reinforcing the need for models tailored to rosette-type configurations.

Numerical simulations have played a central role in advancing understanding of rosette jet dynamics. CFD, in particular, provides an efficient tool to explore a broad range of discharge scenarios and ambient conditions. Various turbulence modeling approaches have been adopted, including Reynolds-averaged Navier–Stokes (RANS) models like the standard and RNG k–ε and k–ω models, which offer good computational efficiency. However, their inherent limitations in capturing unsteady and anisotropic turbulence have led researchers to employ large eddy simulation (LES) and detached eddy simulation (DES) for higher-fidelity modeling of turbulent jet merging and interactions.

To complement and extend laboratory findings, researchers have increasingly used fully three-dimensional CFD models to study buoyant rosette jets. For instance, Yan et al. (2019) developed a CFD framework in OpenFOAM using both standard and RNG k–ε turbulence models to simulate rosette-type discharges. Their results indicated that the RNG k–ε model offered superior accuracy without significantly increasing computational cost. Building upon this, Yan et al. (2021) combined CFD with machine learning techniques to enhance predictive capability. They performed 20 high-resolution CFD simulations under systematically varied ambient density conditions, thereby covering a wide range of densimetric Froude numbers. The simulations were conducted using symmetric boundary conditions to model only one-twelfth of the domain, effectively reducing computational burden while preserving physical accuracy. The CFD model was validated against experimental measurements reported by Lai and Lee (2012), showing good agreement with the model in terms of jet trajectories and near-field normalized concentrations.

Overall, both experimental and numerical approaches have been critical in elucidating the hydrodynamic and scalar transport behavior of rosette-type buoyant jets. While laboratory experiments provide essential reference data for validation, CFD enables detailed investigation of jet dynamics under conditions that are difficult to replicate experimentally. However, the high computational cost of full-domain CFD remains a challenge, particularly for applications requiring parameter sweeps or long-duration simulations. Recent efforts integrating CFD with machine learning, as demonstrated by Yan et al. (2021), offer a promising direction for reducing computational overhead while maintaining predictive accuracy.

2.2 Methodology

A hybrid experimental-computational framework is employed to analyze the behavior of buoyant rosette multi-port jets. Laboratory experiments are conducted in a controlled water tank facility, using laser-induced fluorescence (LIF) technology to capture high-resolution scalar concentration fields and centerline trajectories. Rhodamine fluorescent dye is introduced into the jet to visualize mixing and dilution patterns of rosette standpipe jets under quiescent (zero ambient velocity) conditions. These measurements provide detailed insights into centerline concentration decay, jet trajectory, and the near-field dilution characteristics, forming a reliable validation dataset. Complementary 3D CFD simulations are performed using the OpenFOAM open-source platform, replicating the same standpipe geometry, nozzle configurations, and boundary conditions as those used in the laboratory setup. A series of operating conditions with different density Froude numbers are simulated to systematically investigate the effects of buoyancy, momentum flux ratio, on jet interactions and dilution. The CFD results are compared with experimental LIF data and parameter analysis is performed to ensure the accuracy of the model. This integrated approach enables a comprehensive understanding of the behavior of rosette jets under various hydraulic conditions, laying the foundation for subsequent machine learning model training and predictive analysis.

2.2.1 Experimental methodology

The experimental investigation was conducted using the Laser-Induced Fluorescence (LIF) technique to visualize and quantify the concentration fields and trajectories of buoyant rosette-type jets. The process began with the geometric design of the diffuser using SolidWorks, followed by 3D printing of a four-port rosette-type diffuser. The printed diffuser was then installed inside a transparent experimental tank filled with ambient water.

A planar laser sheet was used as the light source to illuminate the measurement plane, and a fluorescent dye was injected into the jet fluid to enable scalar concentration detection. Prior to data acquisition, the camera and laser system were calibrated.

During each test, more than three thousand sequential fluorescence images were recorded to capture the unsteady mixing behavior of the jet. These images were subsequently processed to obtain time-averaged concentration fields. From the processed data, the jet centerline trajectory (x/D vs. y/D) and normalized concentration distributions were extracted for further comparison with numerical simulation results. The overall workflow of the LIF experimental process is illustrated in Fig. 2.1.

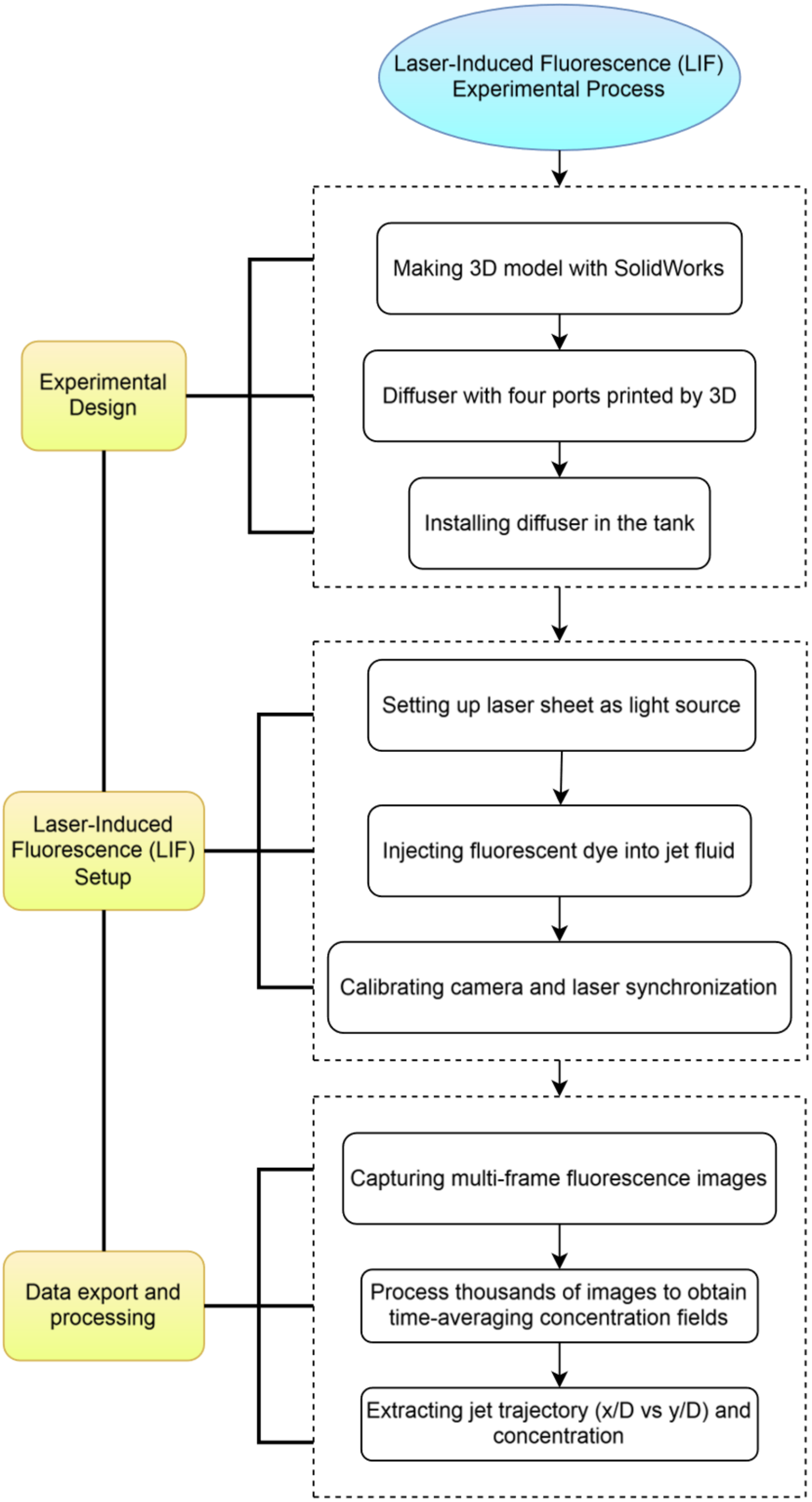

Fig. 2.1 LIF experimental process

2.2.1.1 Experimental facility

The experiment was conducted in the Hydraulics Laboratory at the University of Ottawa, where a test tank, a constant head tank, and a laser light source were installed. Figure 2.2 shows the setup of these equipment schematically. The test tank is made of glass and is 3 m in length, 1.2 m in width, and 1 m in height. The constant head tank located above the test tank maintains the flow into the outlet of the pipe (Figure 2.2 (a)). The flow into the pipe outlet was maintained by a constant-head tank positioned above the test tank. This tank was fed by a storage tank located below it, which pumps a uniform hot rhodamine dye solution. A small mixing pump is installed inside the storage tank to stir the solution before it is pumped upward. The density and temperature of the hot rhodamine dye solution in the storage tank and the fresh water in the test tank were measured and monitored using a portable density meter DMA35 from Anton Paar. A series of experiments with representative ambient and discharge velocities of the rosette jet group ejected from the diffuser were conducted in the tank,

The planar LIF (PLIF) technique was utilized to capture the two-dimensional concentration distribution within the jet flow. During the experiments, the vertical plane along the jet centerline was illuminated by a very thin laser sheet produced by a 5W DPSS Microvec laser used in continues wave mode with a $\lambda_{ex} = 532$ nm, where λ_{ex} is the laser exerted wavelength. The flow dynamics were captured using a FASTEC IL5 camera, equipped with 1080×1920 small ($5\mu m$) pixels and a high-speed CMOS image sensor. A Nikkor lens was mounted on the camera. The camera's compatibility with very low-light environments allowed for an exposure time of 2 ms in 8-bit grayscale mode.

For each experiment, more than 3000 images were recorded at a frame rate of 50 frames per second for a converged time-averaged fully developed flow. To mitigate the effects of ambient light and variations in laser intensity, background images were captured before each measurement with the laser on and the jet off. After each measurement, to ensure that the dye concentration is the same as the previous experiment, add additional dye or fresh water to the container as needed and stir to achieve a uniform concentration. A reference image, with the laser on and the jet off, was then taken. And after each run the test tank was emptied and refilled according to the prescribed procedures of the LIF equipment (Tahmooresi et al., 2025).

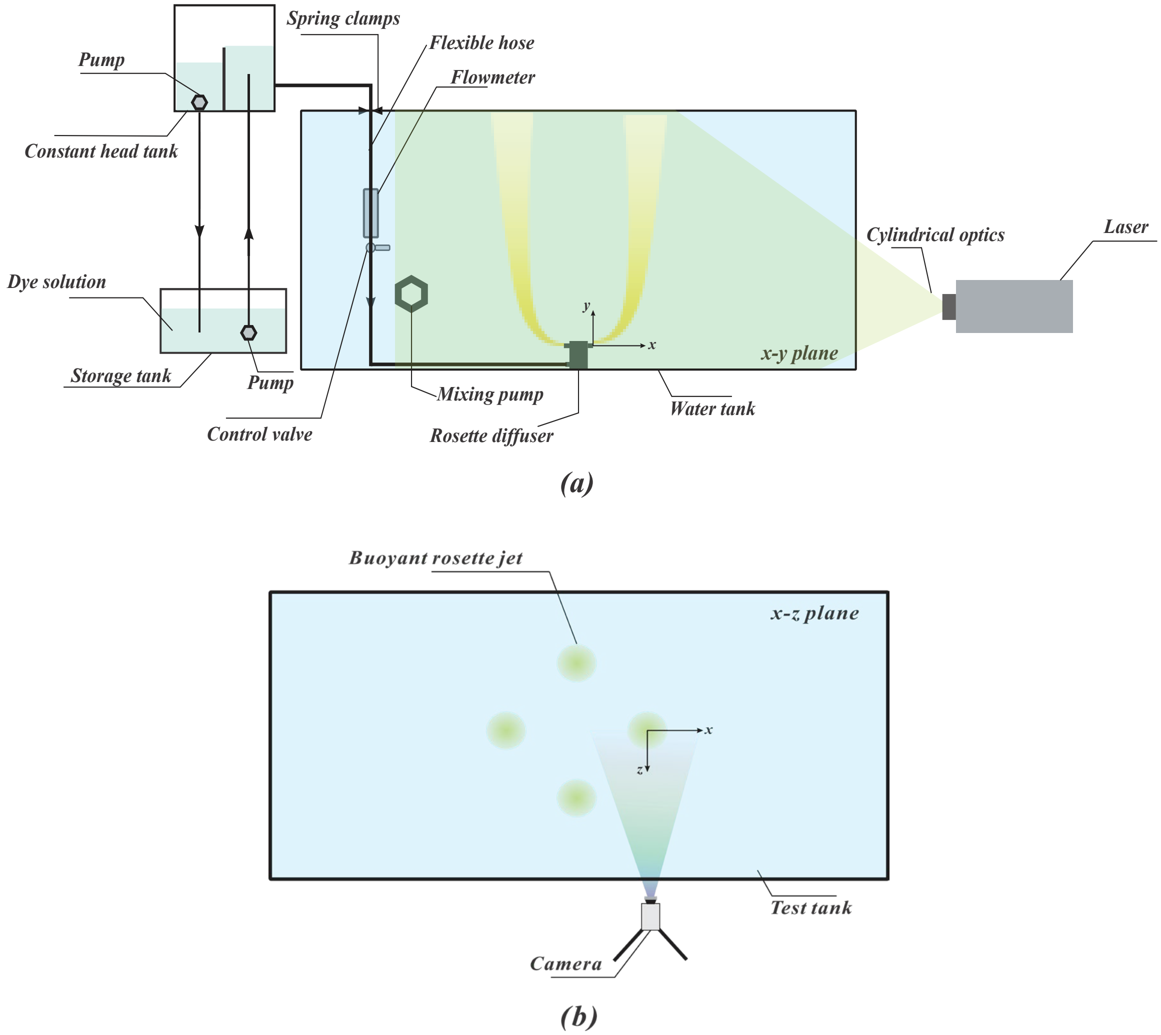

Fig. 2.2 Schematic view of the experimental facility from (a) front view, and (b) top view.

2.2.1.2 Scaling calculations

In order to ensure the representativeness of the model experimental results, this study carried out systematic scaling calculations to ensure the similarity between the model and the prototype in terms of geometry, motion and dynamic characteristics. The prototype parameters were selected based on a literature review of typical rosette diffuser (Table 2.1) operating conditions around the world, covering key parameters such as typical Froude number, nozzle diameter, total flow, number of risers, number of ports, water depth and riser spacing. On this basis, a scaling analysis was carried out to ensure the physical similarity of the model under the influence of geometric similarity, Froude similarity and density ratio. By verifying the scaling relationship of key parameters such as flow, velocity and dimensionless numbers, it is further confirmed that the model experiment can effectively reflect the actual engineering behavior of the prototype, thereby ensuring the scientificity and applicability of the experimental design.

2.1.1.3 Key parameters

The experiments in this study aim to systematically investigate the near-field mixing characteristics of buoyant rosette-shaped multi-port jets in a static water environment. To simulate real discharge conditions, a custom-designed rosette diffuser consisting of a riser and four radially arranged nozzles was fabricated by 3D printing. Laser-induced fluorescence (LIF) was employed to resolve the jet trajectories and concentration profiles. Key parameters of experiments including densimetric Froude number (Fr), Reynolds number (Re), density contrast ($\Delta\rho=\rho_j-\rho_a$), and flow rate. (see Table 2.2 for experiments parameters).

Table 2.1 Prototype parameters of typical rosette diffusers based on global literature review.

Outfall	Fr	nozzle diameter(m)	total discharge(m^3/s)	number of risers	number of ports	h/d	depth (m)	distance between risers	$k=u_0/u_a$	riser diameter	Source
Masan/Changwon (South Korea)	1.47-4.2	0.2	8.23	21	4	65	13	10	5.9-25	1.35	Seo and Yeo (2002)
Onsan (South Korea)	3.98	0.25	1.74	9	4	108	27	18	/	1.35	Seo and Yeo (2002)
Youngyeon(South Korea)	9.8-10.5	0.11-0.125	4.05	48	4	200-245	25-27	10	/	1.35	Seo and Yeo (2002)
Noksan (South Korea)	5	0.5	8.24	6	4	13	6.5	9	3-16.7	1.2	Seo and Yeo (2002)
Sockcho (South Korea)	2.8-4.4	0.225-0.250	1.22	6	4	44-46	10-11.5	10	6.7-20	0.6	Seo and Yeo (2002)
Hong Kong	9.6	0.25	19	24	8	48	12	52	3.4-50.5	2.6	/
North Head (Sydney)	3.6-25.2	0.085-0.185	4.46	36	6	314-682	58	21	2.6-10.8	/	Tate (2002)
Bondi (Sydney)	3.2-29.4	0.085-0.185	1.91	26	4	335-729	62	25	2.3-10.8	/	Tate (2002)
Malabar (Sydney)	4.4-30.9	0.085-0.185	5.67	28	8	427-929	79	25	3.1-14.9	/	Tate (2002)
Boston (US)	10.5-34.0	0.157	17.1-55.7	55	8	205.7325	32.3	37	8.0-54.5	3	Roberts and Snyder (1993a)
San Francisco (US)	3.8-19.1	0.1097-0.1314	6.22-19.72	85	8	174-209	22.9	11	2.6-23.6	1.8	Isaacson et al. (1983)

Table 2.2 Run parameters for rosette buoyant jet LIF experiments in laboratory flume (partial).

Case	$d(m)$	Fr	Re	T_j (℃)	T_a (℃)	$U_j(m/s)$	ρ_j	ρ_a	Flow rate (l/hr)	g'
6	0.0095	5.81	1117	36	20.6	0.118	993.71	998.1	30	0.043
16	0.0095	2.97	745	44	20.6	0.078	990.66	998.1	20	0.073
22	0.0095	2.23	558	44	20.6	0.059	990.66	998.1	15	0.073

The Froude number is defined as:

$$Fr = \frac{U}{\sqrt{g'd}} \tag{2.1}$$

where U is the velocity of the jet, d is the diameter of the nozzle and g' is effective gravitational acceleration, defined as:

$$g' = g\frac{\Delta\rho}{\rho_a} \tag{2.2}$$

where g is gravity acceleration, $\Delta\rho$ is the density difference of ambient water and jet, ρ_a is the density of ambient water.

In the experiments of this study, the density difference $\Delta\rho$ is controlled by the temperature difference between the ambient water and the jet.

2.2.2 CFD simulation methodology

In this section, a comprehensive CFD framework is proposed to complement the experimental results, as shown in Figure 2.3. The diffuser geometry was created as an STL file. The mesh was generated using the snappyHexMesh utility in OpenFOAM, and local refinement was applied in the nozzle area and near the jet trajectory to ensure adequate resolution in the mixing zone. The CFD simulations were performed using a modified version of the *pimpleFoam* solver adapted to handle unsteady buoyancy jets. The numerical time step was dynamically determined by the “adjustableRunTime” codes available in OpenFOAM based on the pre-defined maximum Courant number (See the controlDict file shown in Figure 2.4).

The Reynolds-Averaged Navier-Stokes (RANS) approach was employed to validate the numerical model by comparing the simulated jet trajectory and scalar concentration field with laboratory-scale LIF measurements. Within the RANS framework, three turbulence models were tested: the standard k-ε model, the RNG k-ε model, and the SST k-ω model. The three models were selected based on their unique formulations and their respective strengths in capturing turbulent mixing and buoyancy-driven flow behavior.

The standard k-ε model provides a benchmark representation of turbulent transport and has been widely used in environmental flow simulations. The RNG k-ε model introduces additional terms to account for rapid strain rates and streamline curvature, making it more applicable to complex shear flows and vortex-dominated regions. The SST k-ω model combines the k-ε and k-ω approaches, with improved accuracy in both the near-wall and free-shear regimes, which is particularly important for resolving the interaction region between adjacent jets in rosette-type structures.

Each turbulence model is implemented with the same boundary conditions and geometric settings consistent with the experimental structure. The predicted centerline trajectories (x/D vs. y/D) and normalized scalar concentration profiles are extracted from the simulations and directly compared with the corresponding experimental data. This validation process allows us to quantitatively evaluate the performance of each model in reproducing the key physical features of the rosette jet system.

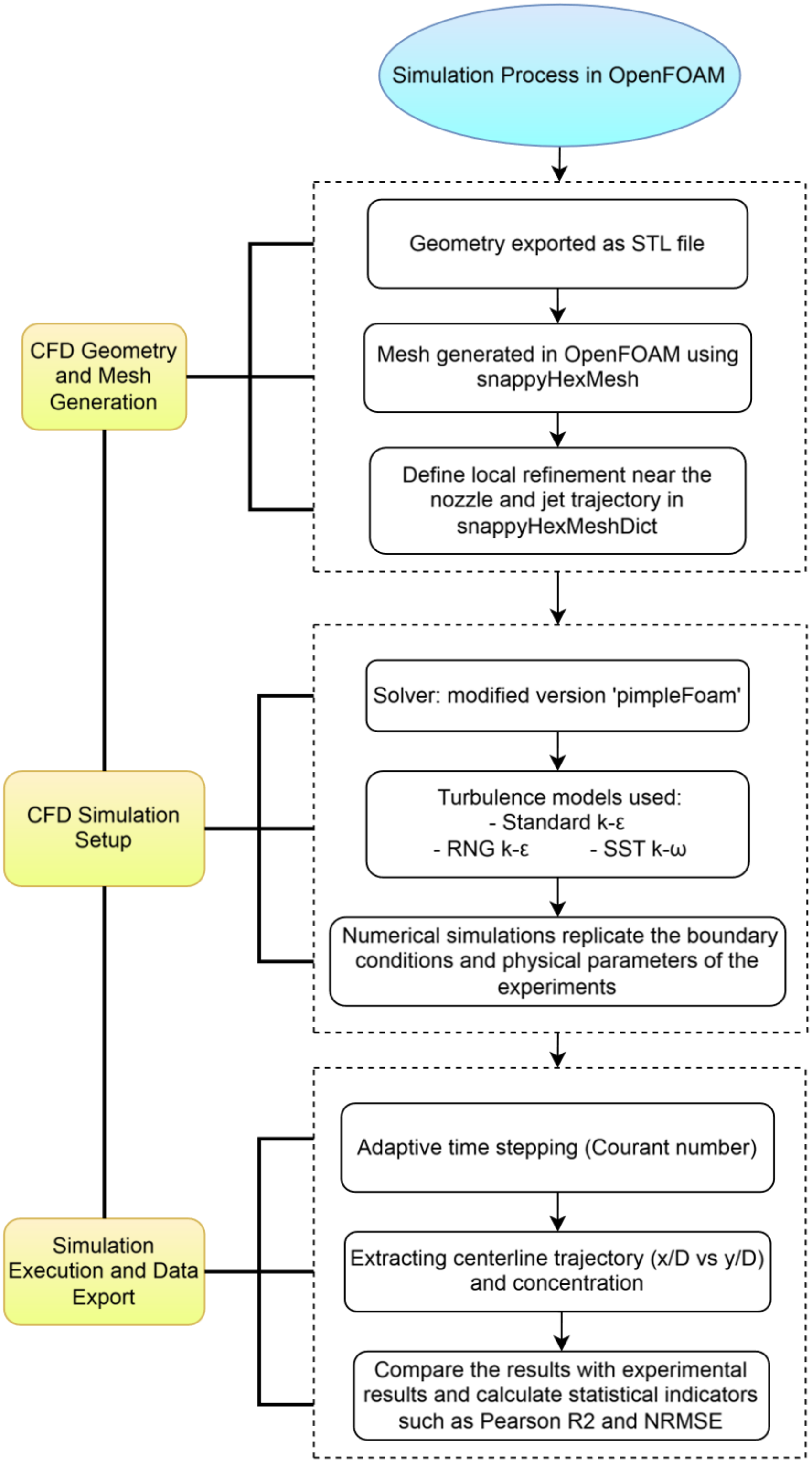

Fig. 2.3 Simulation process in OpenFOAM.

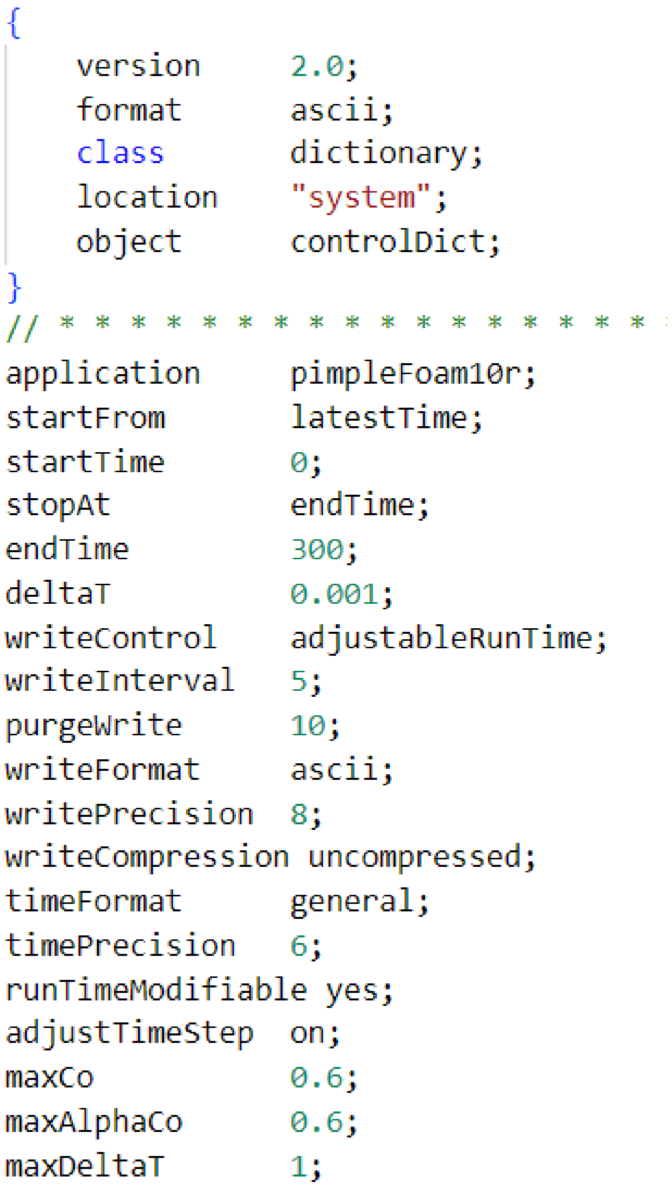

```
{
    version     2.0;
    format      ascii;
    class       dictionary;
    location    "system";
    object      controlDict;
}
// * * * * * * * * * * * * * * * * *
application     pimpleFoam10r;
startFrom       latestTime;
startTime       0;
stopAt          endTime;
endTime         300;
deltaT          0.001;
writeControl    adjustableRunTime;
writeInterval   5;
purgeWrite      10;
writeFormat     ascii;
writePrecision  8;
writeCompression uncompressed;
timeFormat      general;
timePrecision   6;
runTimeModifiable yes;
adjustTimeStep  on;
maxCo           0.6;
maxAlphaCo      0.6;
maxDeltaT       1;
```

Fig. 2.4 ControlDict dictionary.

To further evaluate the model accuracy, statistical metrics such as the normalized root mean square error (NRMSE) and Pearson correlation coefficient squared (R^2) are calculated. These metrics provide an objective measure of how well the numerical results agree with the experimental results and help determine the most appropriate turbulence model for simulating buoyant rose-type multi-port jets under the test conditions.

2.2.3 Numerical model

2.2.3.1 Governing equations

The Navier–Stokes equations are the basic mathematical model for describing the motion of viscous incompressible fluids in fluid dynamics. The core of the equations is a set of partial differential equations for conservation of momentum and mass. The equations have strong nonlinear characteristics with velocity and pressure as the main variables. In particular, the existence of convection terms leads to complex phenomena such as turbulence and vortices. In computational fluid dynamics, the Navier–Stokes equations (especially its incompressible form) form the theoretical basis of most numerical solvers (such as pimpleFoam).

Continuity equations:

$$\frac{\partial u}{\partial x}+\frac{\partial v}{\partial y}+\frac{\partial w}{\partial z}=0 \tag{2.3}$$

Momentum equations:

$$\frac{\partial u}{\partial t}+u\frac{\partial u}{\partial x}+v\frac{\partial u}{\partial y}+w\frac{\partial u}{\partial z}=-\frac{1}{\rho}\frac{\partial P}{\partial x}+\frac{\partial}{\partial x}\left(\upsilon_{eff}\left(\frac{\partial u}{\partial x}\right)\right)+\frac{\partial}{\partial y}\left(\upsilon_{eff}\left(\frac{\partial u}{\partial y}\right)\right)+\frac{\partial}{\partial z}\left(\upsilon_{eff}\left(\frac{\partial u}{\partial z}\right)\right) \tag{2.4}$$

$$\frac{\partial v}{\partial t}+u\frac{\partial v}{\partial x}+v\frac{\partial v}{\partial y}+w\frac{\partial v}{\partial z}=-\frac{1}{\rho}\frac{\partial P}{\partial y}+\frac{\partial}{\partial x}\left(\upsilon_{eff}\left(\frac{\partial v}{\partial x}\right)\right)+\frac{\partial}{\partial y}\left(\upsilon_{eff}\left(\frac{\partial v}{\partial y}\right)\right)+\frac{\partial}{\partial z}\left(\upsilon_{eff}\left(\frac{\partial v}{\partial z}\right)\right)-g\frac{\rho-\rho_0}{\rho} \tag{2.5}$$

$$\frac{\partial w}{\partial t}+u\frac{\partial w}{\partial x}+v\frac{\partial w}{\partial y}+w\frac{\partial w}{\partial z}=-\frac{1}{\rho}\frac{\partial P}{\partial z}+\frac{\partial}{\partial x}\left(\upsilon_{eff}\left(\frac{\partial w}{\partial x}\right)\right)+\frac{\partial}{\partial y}\left(\upsilon_{eff}\left(\frac{\partial w}{\partial y}\right)\right)+\frac{\partial}{\partial z}\left(\upsilon_{eff}\left(\frac{\partial w}{\partial z}\right)\right) \tag{2.6}$$

where u, v and w are the velocity components in the x, y and z directions, respectively; t is the time; P is the fluid pressure; ρ is the fluid density; and ρ_0 is the reference fluid density. υ_{eff} denotes the effective kinematic viscosity, defined as $\upsilon_{eff}=\upsilon+\upsilon_t$, where υ is the molecular kinematic viscosity and υ_t is the turbulent kinematic viscosity calculated from the turbulence model. g represents gravity acceleration. The terms on the left-hand side of the momentum equations describe the transient and convective transport of momentum, while the right-hand side accounts for pressure gradients, viscous diffusion, and buoyancy effects under the Boussinesq approximation.

2.2.3.2 PIMPLE algorithm

OpenFOAM is a widely used open source CFD platform that provides a range of solvers and libraries for fluid flow, turbulence, and scalar transport modeling. *pimpleFoam* is a transient solver designed for incompressible turbulent flows that combines the advantages of the PISO and SIMPLE algorithms, allowing the numerical stability of the simulation to be maintained when using large time steps. It can be used in conjunction with LES and RANS turbulence models. Figure 2.6 shows the PIMPLE algorithm flow chart, which is a merged PISO-SIMPLE algorithm for pressure-velocity coupled problems (Roohi et al., 2016).

In order to simulate unsteady incompressible flows involving complex boundary conditions and turbulence effects, this study uses the *pimpleFoam* solver as a benchmark to modify the solver. *pimpleFoam* is a transient solver implemented in the OpenFOAM framework. It is based on the PIMPLE method and combines the advantages of the SIMPLE (semi-implicit method of pressure-related equations) and PISO (pressure implicit method by operator splitting) algorithms. The core of this solver is based on the PISO algorithm proposed by Issa (1986), which proposes a non-iterative operator splitting method for decoupling the pressure-velocity coupling in the solution of the Navier-Stokes equations. This method implements implicit time stepping and improves the numerical stability and efficiency of large time steps, making it particularly suitable for transient simulations.

Over the years, *pimpleFoam* has been widely verified and applied in various incompressible flow scenarios, including rotating machinery, multiphase systems, and buoyant jets. For example, Tukovic and Jasak (2012) extended the applicability of the PIMPLE algorithm to arbitrary mesh motions using a cell center-based finite volume method. In addition, the performance and accuracy of *pimpleFoam* in large eddy simulation and Reynolds-averaged Navier-Stokes (RANS) turbulence modeling have been verified in typical applications and engineering applications (Weller et al., 1998; Moukalled et al., 2016). In the field of buoyant jet modeling, Wu et al. (2021) successfully demonstrated the applicability of *pimpleFoam* in simulating transverse buoyant jet-induced mixed convection, confirming its reliability in capturing complex flow structure transitions and hysteresis phenomena under varying buoyancy and inertial forces.

These advances highlight *pimpleFoam* as a robust and flexible solver that can capture the key dynamics of unsteady, turbulent, incompressible flows, thus justifying its selection in this study.

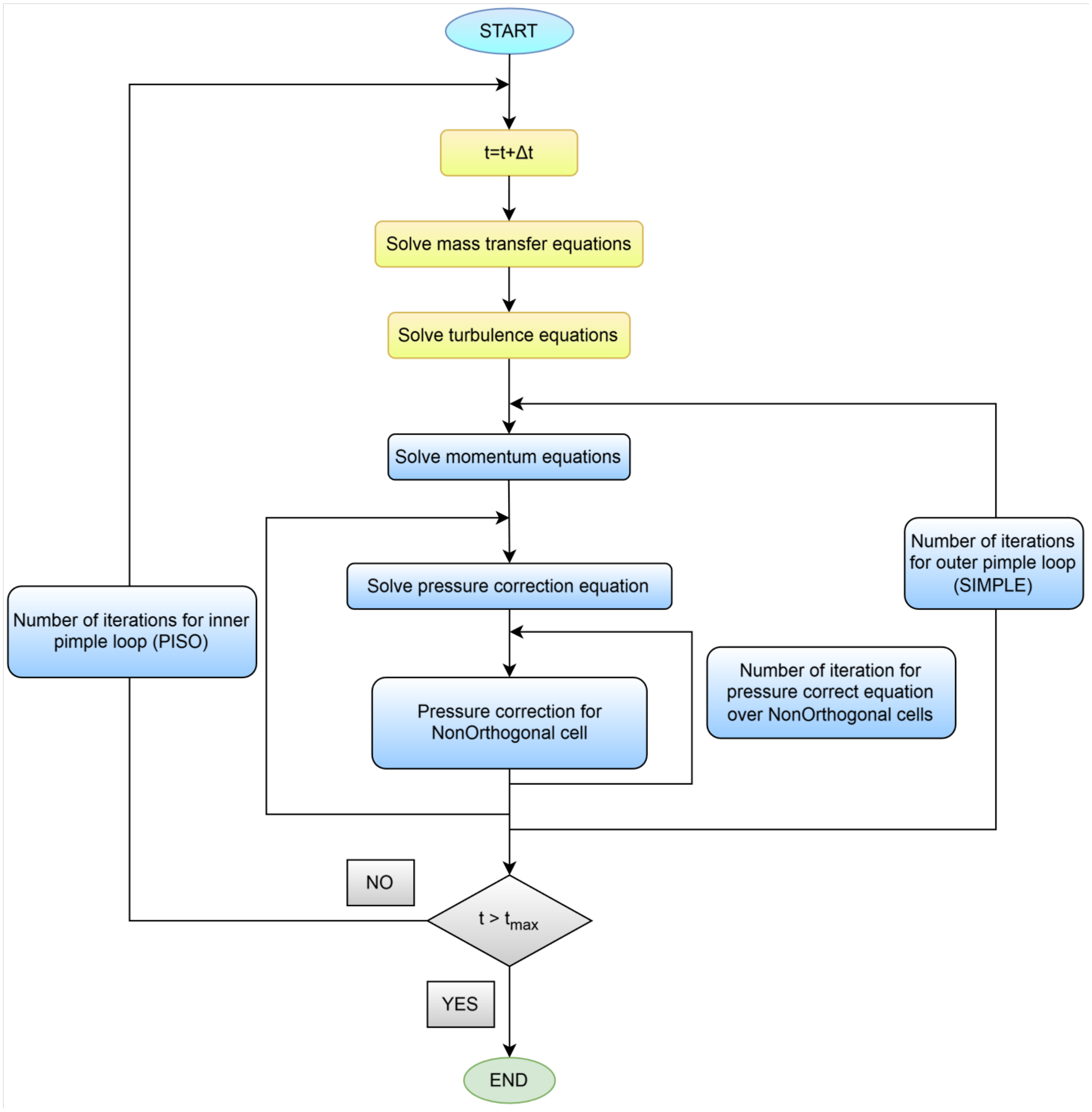

Fig. 2.5 PIMPLE flowchart (based on Roohi et al., 2016).

2.2.3.3 Density calculation

All simulations in this study used a custom modified version of the OpenFOAM transient solver pimpleFoam, which is not an official OpenFOAM solver but has been extended to support thermally driven buoyancy flows. The modified solver retains the structure of the original pimpleFoam algorithm PIMPLE, which is a merger of PISO-SIMPLE for solving pressure-velocity coupled problems for incompressible transient turbulent flows. To be able to simulate scalar transport phenomena, the convection-diffusion equations for temperature and salinity (or concentration) are incorporated into the solver framework.

The original pimpleFoam solver uses the empirical equation of state for seawater proposed by Millero and Poisson (1981), which is commonly used to determine the density of a jet and its surrounding water body, modeling the density as a nonlinear function of temperature T and salinity S, including linear and higher-order terms for salinity. The complete expression is as follows:

$$\rho = \rho_t + AS + BS^{3/2} + CS \tag{2.7}$$

where,

$$\begin{aligned} A &= 8.24493\times10^{-1} - 4.0899\times10^{-3}T + 7.6438\times10^{-5}T^2 - 8.2467\times10^{-7}T^3 + 5.3875\times10^{-9}T^4 \\ B &= -5.72466\times10^{-3} + 1.0227\times10^{-4}T - 1.6546\times10^{-6}T^2 \\ C &= 4.8314\times10^{-4} \end{aligned} \tag{2.8}$$

and ρ_t is the density of water that varies with the temperature (T), as follows:

$$\begin{aligned} \rho_t = {} & 999.842594 + 6.793952\times10^{-2}T - 9.095290\times10^{-3}T^2 + \\ & 1.001685\times10^{-4}T^3 - 1.120083\times10^{-6}T^4 + 6.536336\times10^{-9}T^5 \end{aligned} \tag{2.9}$$

This formulation accounts for the nonlinear dependence of seawater density on both temperature and salinity. However, in the customized solver pimpleFoam10r, salinity transport is deliberately omitted to reduce computational cost. Although the salinity field S is initialized and included in the density expression, it is statically assigned a uniform value of zero throughout the domain (see the 0/S file shown in Fig. 2.6), and its transport equation is not activated in the solver (see commented section in pimpleFoam10r.C shown in Fig. 2.7). Therefore, the salinity-related terms in Eq. (2.7) become numerically negligible, and the effective density simplifies to a function of temperature only:

$$\rho = \rho_t \tag{2.10}$$

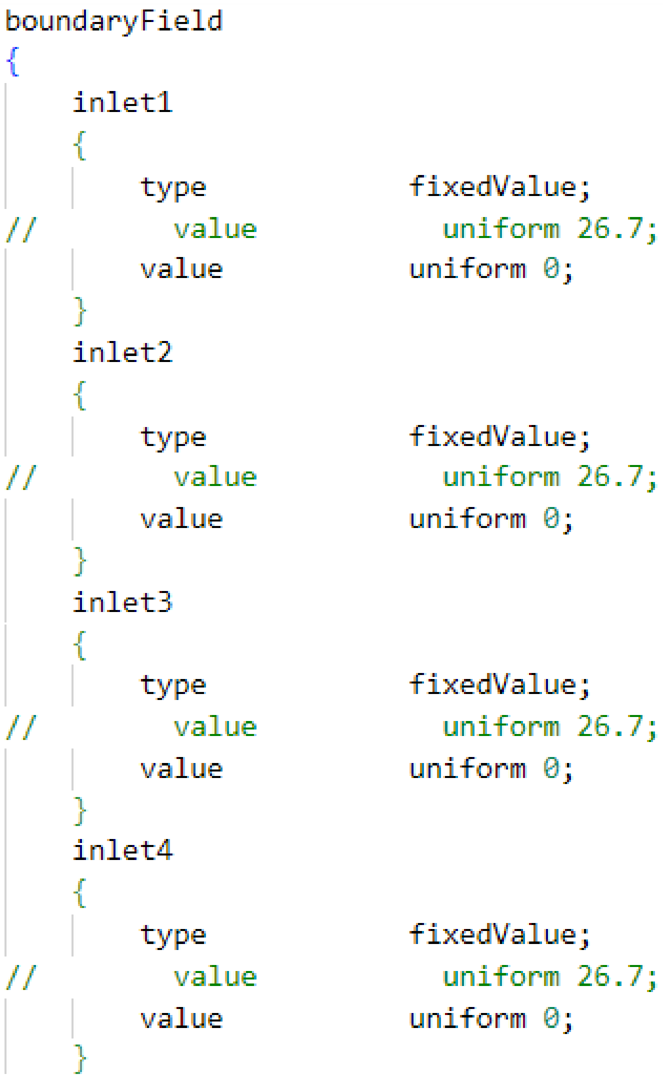

```
boundaryField
{
    inlet1
    {
        type            fixedValue;
//          value           uniform 26.7;
        value           uniform 0;
    }
    inlet2
    {
        type            fixedValue;
//          value           uniform 26.7;
        value           uniform 0;
    }
    inlet3
    {
        type            fixedValue;
//          value           uniform 26.7;
        value           uniform 0;
    }
    inlet4
    {
        type            fixedValue;
//          value           uniform 26.7;
        value           uniform 0;
    }
```

Fig. 2.6 BoundaryField in 0/S file.

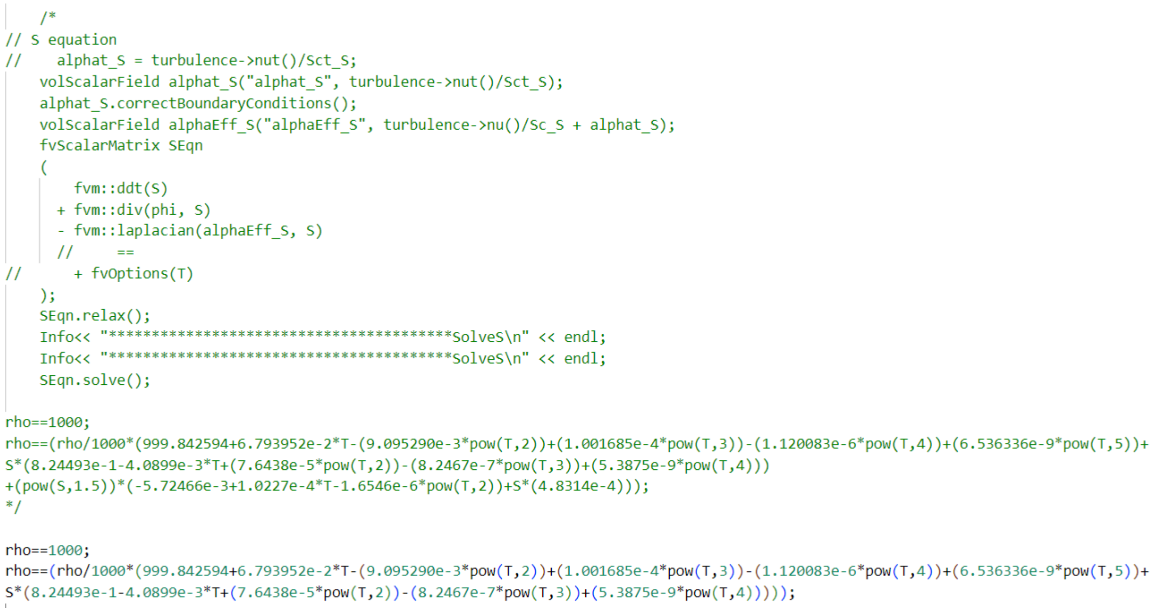

```
    /*
// S equation
//    alphat_S = turbulence->nut()/Sct_S;
    volScalarField alphat_S("alphat_S", turbulence->nut()/Sct_S);
    alphat_S.correctBoundaryConditions();
    volScalarField alphaEff_S("alphaEff_S", turbulence->nu()/Sc_S + alphat_S);
    fvScalarMatrix SEqn
    (
        fvm::ddt(S)
      + fvm::div(phi, S)
      - fvm::laplacian(alphaEff_S, S)
      //     ==
//      + fvOptions(T)
    );
    SEqn.relax();
    Info<< "****************************************SolveS\n" << endl;
    Info<< "****************************************SolveS\n" << endl;
    SEqn.solve();

rho==1000;
rho==(rho/1000*(999.842594+6.793952e-2*T-(9.095290e-3*pow(T,2))+(1.001685e-4*pow(T,3))-(1.120083e-6*pow(T,4))+(6.536336e-9*pow(T,5))+
S*(8.24493e-1-4.0899e-3*T+(7.6438e-5*pow(T,2))-(8.2467e-7*pow(T,3))+(5.3875e-9*pow(T,4)))
+(pow(S,1.5))*(-5.72466e-3+1.0227e-4*T-1.6546e-6*pow(T,2))+S*(4.8314e-4)));
*/

rho==1000;
rho==(rho/1000*(999.842594+6.793952e-2*T-(9.095290e-3*pow(T,2))+(1.001685e-4*pow(T,3))-(1.120083e-6*pow(T,4))+(6.536336e-9*pow(T,5))+
S*(8.24493e-1-4.0899e-3*T+(7.6438e-5*pow(T,2))-(8.2467e-7*pow(T,3))+(5.3875e-9*pow(T,4)))));
```

Fig. 2.7 Simplified density calculations and annotations for the salinity transport equation in the pimpleFoam10r.C.

As a result, buoyancy forces in the simulation are solely driven by temperature gradients. This simplification is appropriate when salinity differences between the jet and ambient fluid are negligible, as is the case in the present configuration.

2.2.3.4 Turbulence models

It is widely accepted among researchers in the field that no single turbulence model can be universally applied to all situations. Some considerations must be considered when choosing a turbulence model, including the physics encompassed in the flow, the level of accuracy, and the computational resources available. In order to evaluate the performance of different turbulence models for dense jet discharges, three turbulence models were initially considered in this study, namely (i) the Standard k-ε model, (ii)the RNG k-ε model, and (iii) the SST k-ω model.

The Standard k-ε model was proposed by Launder and Spalding (1972). In this model, the transport equation for the turbulent kinetic energy (*k*) is derived from the momentum equation. However, the transport equation for the turbulent kinetic energy dissipation (*ε*) is derived by physical reasoning and is similar to the mathematically derived transport equation for k. The turbulent kinetic energy and its dissipation rate in this model are given by:

$$\frac{\partial k}{\partial t}+\frac{\partial k u_i}{\partial x_i}=\frac{\partial}{\partial x_i}(Dk_{eff}\frac{\partial k}{\partial x_i})+G_k-\varepsilon \tag{2.11}$$

$$\frac{\partial \varepsilon}{\partial t}+\frac{\partial \varepsilon u_i}{\partial x_i}=\frac{\partial}{\partial x_i}(D\varepsilon_{eff}\frac{\partial \varepsilon}{\partial x_i})+C_{1\varepsilon}\frac{\varepsilon}{k}G_k-C_{2\varepsilon}\frac{\varepsilon^2}{k} \tag{2.12}$$

where G_k represents the generation of turbulent kinetic energy due to mean velocity gradients and Dk_{eff} and $D\varepsilon_{eff}$ are the effective diffusivity for *k* and *ε*, respectively. Their values are calculated as

$$Dk_{eff}=\nu+\nu_t \tag{2.13}$$

$$D\varepsilon_{eff}=\nu+\frac{\nu_t}{\sigma_\varepsilon} \tag{2.14}$$

The turbulent kinematic viscosity at each point is related to the local values of turbulent kinetic energy and its dissipation rate by

$$\nu_t=C_\mu\frac{k^2}{\varepsilon} \tag{2.15}$$

σ_ε is turbulent Prandtl number for *ε*. This value has been determined experimentally and is assumed equal to 1.3.

$C_{1\varepsilon}$, $C_{2\varepsilon}$ and C_μ are constants that have also been derived experimentally and are chosen to have the following values

$C_{1\varepsilon}=1.44,\ C_{2\varepsilon}=1.92,\ C_\mu=0.09$

The term for the production of turbulent kinetic energy G_k is common in most turbulence models and is defined as

$$G_k=-\overline{u_i^{'}u_j^{'}}\frac{\partial u_j}{\partial u_i} \tag{2.16}$$

This can also be written as

$$G_k=2\nu_t S_{ij}^{\ 2} \tag{2.17}$$

$$S_{ij} = 0.5(\frac{\partial u_j}{\partial x_i} + \frac{\partial u_i}{\partial x_j}) \tag{2.18}$$

where $u_i^{'}$, $u_j^{'}$ and S_{ij} are the fluctuating parts of velocity and strain-rate tensor respectively.

Similar to the standard k-ε model, the RNG model is derived from the transient Navier-Stokes equations, except that it uses the renormalization group theory technique described by Yakhot and Orszag (1986). The derivation they used produces a different constant model from that in the standard k-ε model and adds new terms to the transport equations for turbulent kinetic energy and its dissipation. The RNG model also takes into account the effects of eddies, which improves the accuracy of eddy flows. The model provides an analytical formula for the turbulent Prandtl number, while the standard model relies on user-defined constant values. Finally, assuming that the near-wall region is properly treated, the RNG model uses an analytically derived differential formula for the effective turbulent viscosity that can account for low Reynolds number flows. Due to these differences, the transport equation can be written as

$$\frac{\partial k}{\partial t} + \frac{\partial k u_i}{\partial x_i} = \frac{\partial}{\partial x_i}(Dk_{eff}\frac{\partial k}{\partial x_i}) + G_k - \varepsilon \tag{2.19}$$

$$\frac{\partial \varepsilon}{\partial t} + \frac{\partial \varepsilon u_i}{\partial x_i} = \frac{\partial}{\partial x_i}(D\varepsilon_{eff}\frac{\partial \varepsilon}{\partial x_i}) + (C_{1\varepsilon} - R)\frac{\varepsilon}{k}G_k - \frac{C_{2\varepsilon}\varepsilon^2}{k} \tag{2.20}$$

Some terms are obtained differently from the standard model. Dk_{eff} is calculated as

$$Dk_{eff} = \upsilon + \frac{\upsilon_t}{\sigma_k} \tag{2.21}$$

The renormalization term, *R*, is formulated as

$$R = \frac{\eta(1 - \frac{\eta}{\eta_0})}{1 + \beta\eta^3} \tag{2.22}$$

$$\eta = S_{ij}\frac{k}{\varepsilon} \tag{2.23}$$

All model constants are defined as

$$C_\mu = 0.0845,\ C_{1\varepsilon} = 1.42,\ C_{2\varepsilon} = 1.68,\ \sigma_k = 0.71942,\ \sigma_\varepsilon = 0.71942,\ \eta_0 = 4.38,\ \beta = 0.012.$$

The shear stress transport k-ω model is another RANS model. This model was developed by Menter (1994) based on the standard k-ω model and a modified k-ε model. The main difference is the way the model computes the turbulent viscosity to account for the main turbulent shear stress transport. The model also introduces a cross-diffusion term in the ω equation and a mixing function to correctly compute the near-wall and far-field regions. The mixing function triggers the standard k-ω model in the near-wall region and the k-ε model in the region far from the surface.

The transport equations for k and ω are given by

$$\frac{\partial k}{\partial t}+\frac{\partial k u_i}{\partial x_i}=\frac{\partial}{\partial x_i}(Dk_{eff}\frac{\partial k}{\partial x_i})+G_k-\beta^* k\omega \tag{2.24}$$

$$\frac{\partial \omega}{\partial t}+\frac{\partial \omega u_i}{\partial x_i}=\frac{\partial}{\partial x_i}(D\omega_{eff}\frac{\partial \omega}{\partial x_i})+2\gamma S_{ij}-\beta\omega^2+(1-F_1)CD_{k\omega} \tag{2.25}$$

Where G_k represents the generation of turbulent kinetic energy due to mean velocity gradients and is calculated as

$$G_k=\min(2\upsilon_t S_{ij}, C_1\beta^*\omega k) \tag{2.26}$$

Dk_{eff}, $D\omega_{eff}$, υ_t, F_1 and F_2 are also formulated as

$$Dk_{eff}=\upsilon+\alpha_k\upsilon_t \tag{2.27}$$

$$D\omega_{eff}=\upsilon+\alpha_\omega\upsilon_t \tag{2.28}$$

$$\upsilon_t=\frac{a_1 k}{\max(a_1\omega, S_{ij}F_2)} \tag{2.29}$$

$$F_1=\tanh\left[\left[\min\left[\min\left[\max(\frac{\sqrt{k}}{\beta^*\omega y},\frac{500\upsilon}{y^2\omega}),\frac{4\alpha_{\omega2}k}{CD_{k\omega^+}y^2}\right],10\right]\right]^4\right] \tag{2.30}$$

$$CD_{k\omega^+}=\max(CD_{k\omega},10^{-10}) \tag{2.31}$$

$$CD_{k\omega}=2\alpha_{\omega2}\frac{1}{\omega}\frac{\partial k}{\partial x_i}\frac{\partial \omega}{\partial x_i} \tag{2.32}$$

$$F_1 = \tanh\left[\left[\max\left(\frac{2\sqrt{k}}{\beta^{*}\omega y},\frac{500\upsilon}{y^{2}\omega}\right)\right]^{2}\right] \tag{2.33}$$

The constants specific to the SST k-ω model are defined as

$A_1 = 0.31,\ \alpha_{k1} = 0.85034,\ \alpha_{k2} = 1,\ \alpha_{\omega 1} = 0.5,\ \alpha_{\omega 2} = 0.85616,\ \beta_1 = 0.075,\ \beta_2 = 0.0828,\ \beta^{*} = 0.09,$
$\gamma_1 = 0.05532,\ \gamma_1 = 0.4403.$

2.2.3.5 Computational Domain and Boundary Conditions

The full domain of the buoyant rosette is considered in this study. The computational domain is meshed using the snappyHexMesh utility in OpenFOAM, which generates a compliant, hexahedral dominated, locally refined mesh, especially in the region near the nozzle outlet (see Figure 2.8(c)) to ensure adequate resolution of velocity and concentration gradients. Multiple levels of mesh refinement are set up through the refinementSurfaces and refinementRegions commands (Figure 2.9 shows snappyHexMeshDict) to accurately resolve key geometric features and local flow behavior.

The accuracy and stability of the simulation are strongly influenced by the prescribed boundary conditions, which are defined for velocity(U), pressure(P), temperature(T), turbulence quantities (k, epsilon) and other transported scalars.

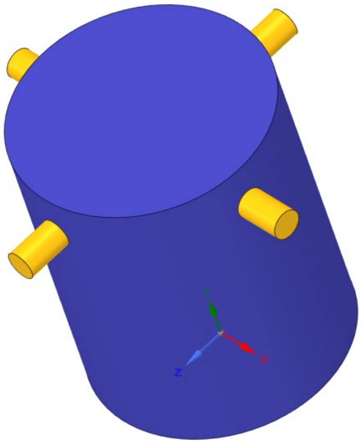

(a)

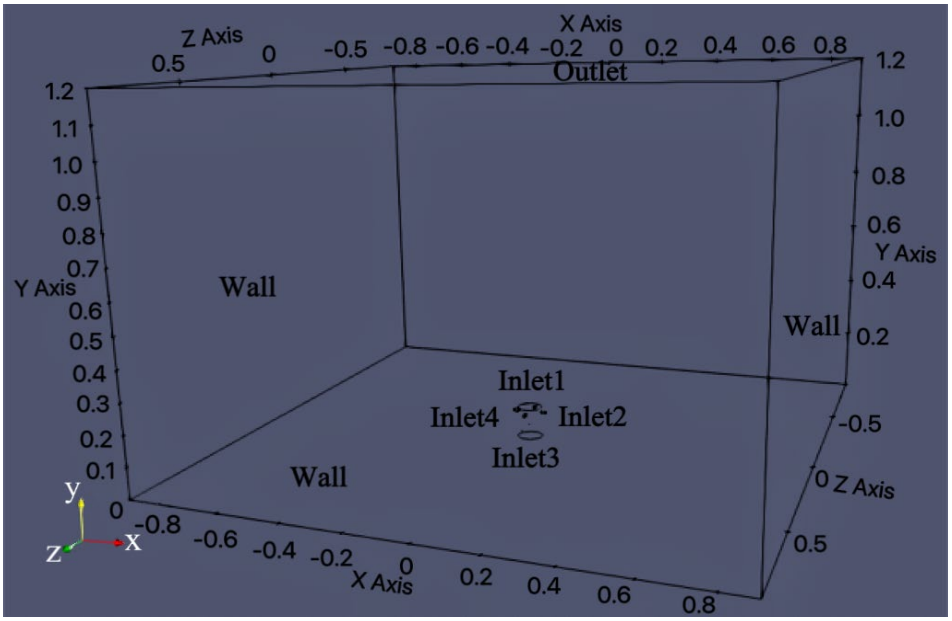

(b)

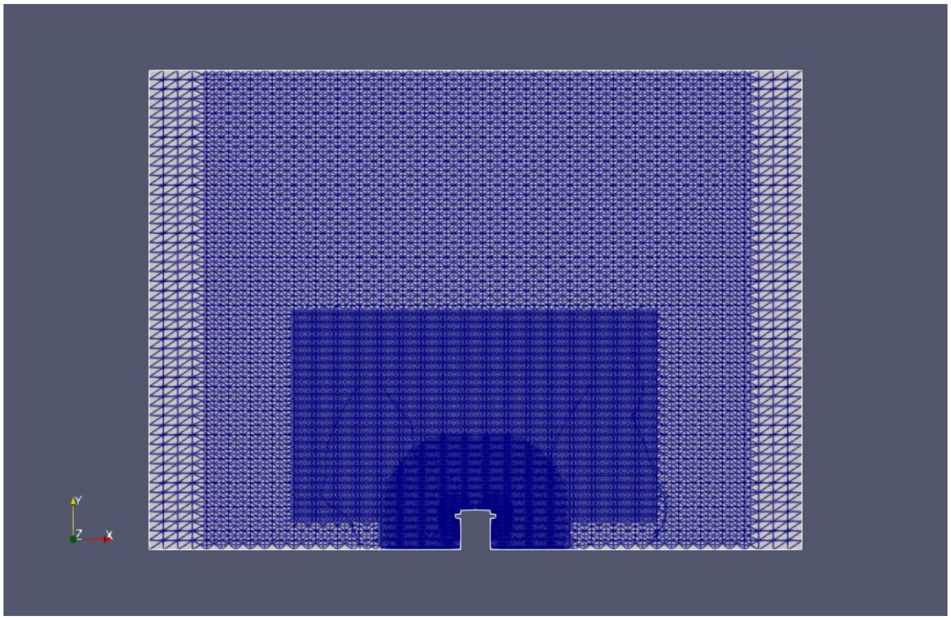

(c)

Fig. 2.8 Rosette diffuser, Computational domain, and mesh: (a) a schematic of the diffuser (b) domain dimensions and boundary conditions of the numerical model (c) a refined mesh of the slice.

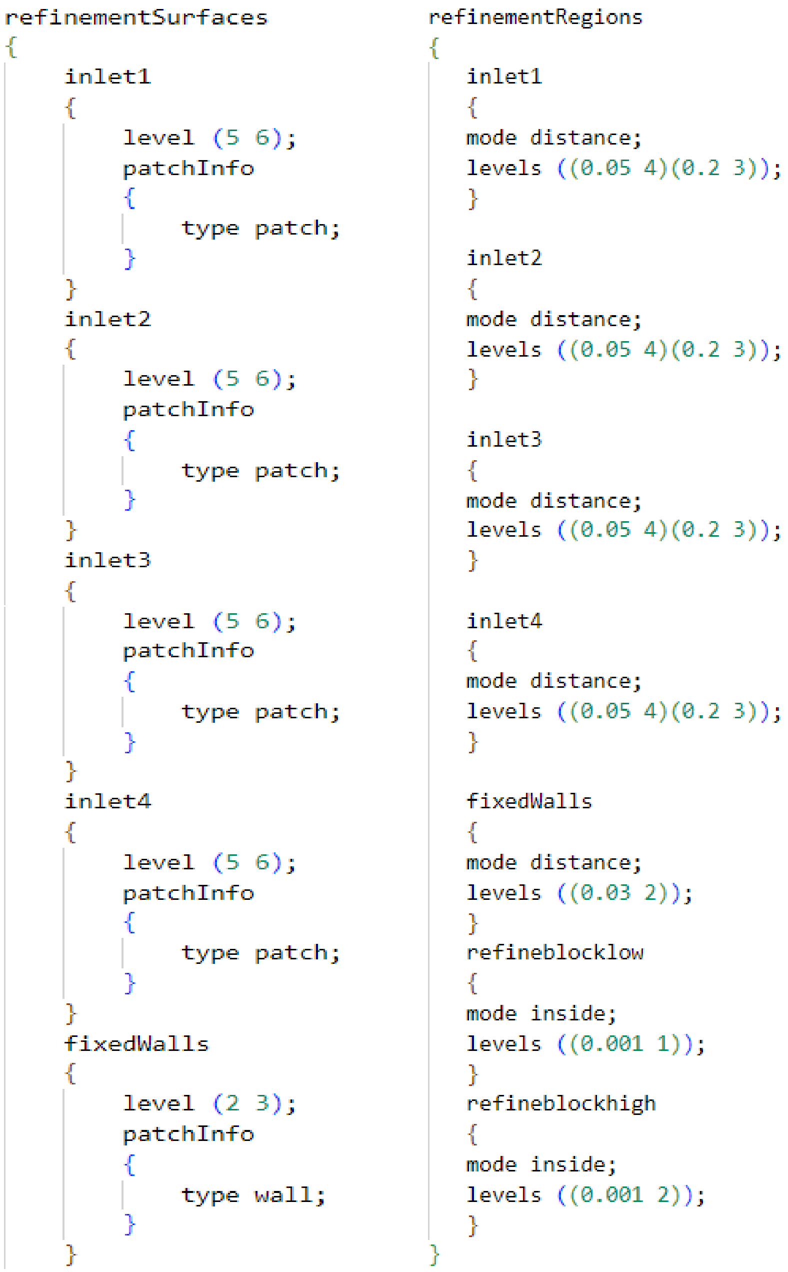

```
refinementSurfaces
{
    inlet1
    {
        level (5 6);
        patchInfo
        {
            type patch;
        }
    }
    inlet2
    {
        level (5 6);
        patchInfo
        {
            type patch;
        }
    }
    inlet3
    {
        level (5 6);
        patchInfo
        {
            type patch;
        }
    }
    inlet4
    {
        level (5 6);
        patchInfo
        {
            type patch;
        }
    }
    fixedWalls
    {
        level (2 3);
        patchInfo
        {
            type wall;
        }
    }
```

```
refinementRegions
{
   inlet1
   {
   mode distance;
   levels ((0.05 4)(0.2 3));
   }

   inlet2
   {
   mode distance;
   levels ((0.05 4)(0.2 3));
   }

   inlet3
   {
   mode distance;
   levels ((0.05 4)(0.2 3));
   }

   inlet4
   {
   mode distance;
   levels ((0.05 4)(0.2 3));
   }

   fixedWalls
   {
   mode distance;
   levels ((0.03 2));
   }
   refineblocklow
   {
   mode inside;
   levels ((0.001 1));
   }
   refineblockhigh
   {
   mode inside;
   levels ((0.001 2));
   }
}
```

Fig. 2.9 SnappyHexMeshDict dictionary.

Take case 22 as an example, for the inlet1 - 4 (nozzle), the boundary conditions are: inlet1: $u_1=0$, $v_1=0$, $w_1=-0.058782989$; inlet2: $u_2=0.058782989$, $v_2=0$, $w_2=0$; inlet3: $u_3=0$, $v_3=0$, $w_3=0.058782989$; inlet4: $u_4=0.058782989$, $v_4=0$, $w_4=0$. Where, U is velocity of jet, u, v and w are the velocity for x, y and z-axis respectively. The inlet values for T, k, ε and ω is $T=T_0$, $k=0.06u^2$, $\varepsilon=0.006u^3/D$ (as mentioned in section 2.2, D = 0.0095m) and $\omega=\varepsilon/k$. T represents temperature, which is the same as the ambient water. The entire computational domain was initially filled with quiescent ambient water at a uniform temperature of 20.6 °C (Kheirkhah Gildeh, 2013; Huai et al., 2010).

At the outlet, a zero-gradient boundary condition was applied for all variables, including velocity components, turbulence quantities, and transported scalars, ensuring that the flow could freely exit the domain without artificial reflection.

For the wall boundaries, a no-slip condition was used for the velocity field. The turbulence quantities k and ε were treated using standard wall functions, ensuring appropriate near-wall behavior in the RANS turbulence framework. For simulations using the SST k-ω model, the turbulent frequency ω was also assigned wall-function treatment, and v_t was evaluated accordingly.

2.2.3.6 Mesh Sensitivity Analysis

The mesh quality is important for the numerical modeling results (Wang & Mohammadian, 2020). To evaluate the effect of mesh resolution on simulation accuracy, a mesh sensitivity analysis was performed. Following the approach of Yan and Mohammadian (2017, 2019), three mesh densities—coarse, medium, and fine—were tested. The total number of cells, the minimum cell size in the refined region, and the overall resolution varied for each mesh density, as shown in Table 2.3.

Table 2.3 Mesh statistics and quality metrics for coarse, medium, and fine grids

Mesh quantity	cells	Min volume	Max volume	Max aspect ratio	Max skewness
Coarse	1491032	5.45013×10^{-10}	5.40×10^{-5}	4.0702546	3.7564077
Medium	2072860	3.17011×10^{-10}	3.84×10^{-5}	4.2144428	2.4518439
Fine	2496178	3.01618×10^{-10}	3.25×10^{-5}	4.1730038	2.3633953

For each mesh configuration, the same turbulence model (RNG k-ε) and boundary conditions were used for the simulations.

To verify the sensitivity of the simulation results to the mesh resolution, a systematic mesh sensitivity analysis was conducted. Three groups of mesh models with different resolutions were constructed and compared: coarse mesh, medium mesh (as a benchmark), and fine mesh. When extracting data from simulated results images, the grayscale values in the image are converted to concentration values through linear normalization. Select a white point (highest concentration) and a black point (lowest concentration) in the image as references, and set their grayscale values as $G_{\max}$ and $G_{\min}$, then the normalized concentration calculation formula for any pixel point is:

$$\widehat{C} = 1 - \frac{G - G_{\min}}{G_{\max} - G_{\min}} \tag{2.34}$$

Where G is the grayscale value of the pixel, and $G_{\min}$ and $G_{\max}$ are the grayscale values of the two reference points. This method can effectively convert image information into concentration distribution and keep it within the range of [0,1].As shown in Figure 2.10, by comparing and analyzing key parameters such as concentration and trajectory, it was found that the difference in simulation results between medium mesh and fine mesh can be ignored, indicating that the medium-resolution mesh can meet the numerical accuracy requirements. Therefore, this medium-resolution mesh configuration considers computational efficiency while ensuring simulation accuracy and was eventually selected for subsequent simulation studies.

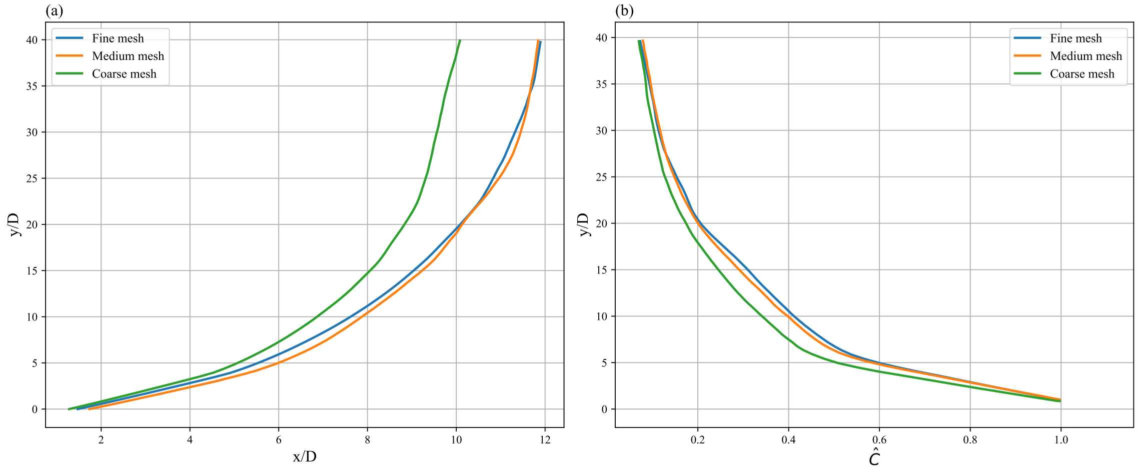

Fig. 2.10 Effect of mesh resolution on jet trajectory (x/D vs y/D) and normalized concentration ($\hat{C}$ vs y/D).

The results show that the coarse mesh cannot accurately resolve the near-field jet structure, resulting in significant deviations in both the trajectory and the scalar field. The fine mesh provides very detailed and accurate predictions, but at a high computational cost. The results for the medium mesh are comparable to those for the fine mesh while maintaining computational efficiency. Based on these observations, the medium resolution mesh was chosen for all subsequent simulations to ensure the best balance between accuracy and cost.

This mesh independence verification ensures that the numerical predictions of the jet dynamics and concentration field are not significantly affected by further mesh refinement, thus increasing the confidence in the CFD results presented in the following sections.

2.3 Result and discussion

This section aims to systematically evaluate the prediction capabilities of three turbulence models (Standard k-ε, RNG k-ε, SST k-ω) for the jet trajectory and concentration in the process of simulating rose petal-shaped buoyancy jets. As shown in Figures 2.11 and 2.12, the laser induced fluorescence (LIF) technique captured the concentration distribution of the jet under two representative cases (Case 6 and Case 22). Fig. 2.11 presents the normalized time-averaged concentration field, obtained by averaging over more than 3,000 instantaneous images recorded by the high-resolution camera during the experiment. This provides a clear visualization of the mean trajectory and spreading behavior of the buoyant jet. Figure 2.12 shows a representative instantaneous normalized concentration map, which reveals the unsteady and turbulent structures in the flow field, particularly highlighting the mixing layers and eddy formations characteristic of buoyant jet dynamics. These experimental visualizations serve as a qualitative reference for evaluating the accuracy and physical fidelity of the numerical simulations. By comparing with the results of laser induced fluorescence (LIF) experiments, the results obtained by simulation using different models are selected when y/D=0 - 40, and the fitting error statistics of the experimental and simulated centerline position of the trajectory (x/D vs. y/D) and normalized concentration are performed. The Pearson correlation coefficient square (R^2) and the normalized root mean square error (NRMSE) (defined as Equations 2.35 - 2.36) are calculated to quantify the differences in the prediction accuracy of each model. The analysis focuses on comparing experimental and simulated results at corresponding y/D positions. By evaluating the differences in x/D and normalized concentration at each matched location, the accuracy and applicability of each turbulence model in predicting jet trajectories and scalar transport are quantitatively assessed. Furthermore, the strengths and limitations of each model under different jet conditions are systematically discussed.

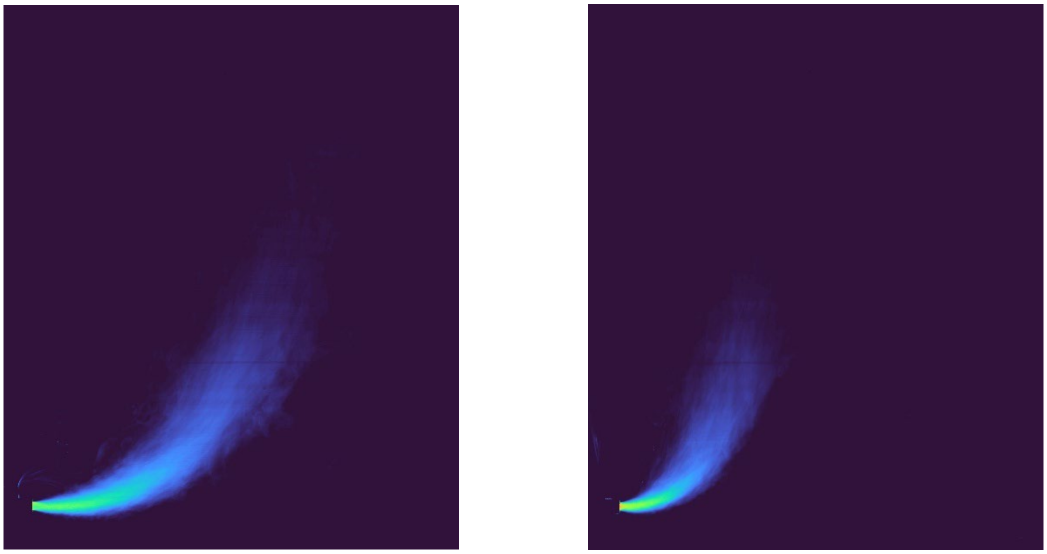

(a) (b)

Fig. 2.11 Normalized time-averaged concentration: (a) case 6, (b) case 22.

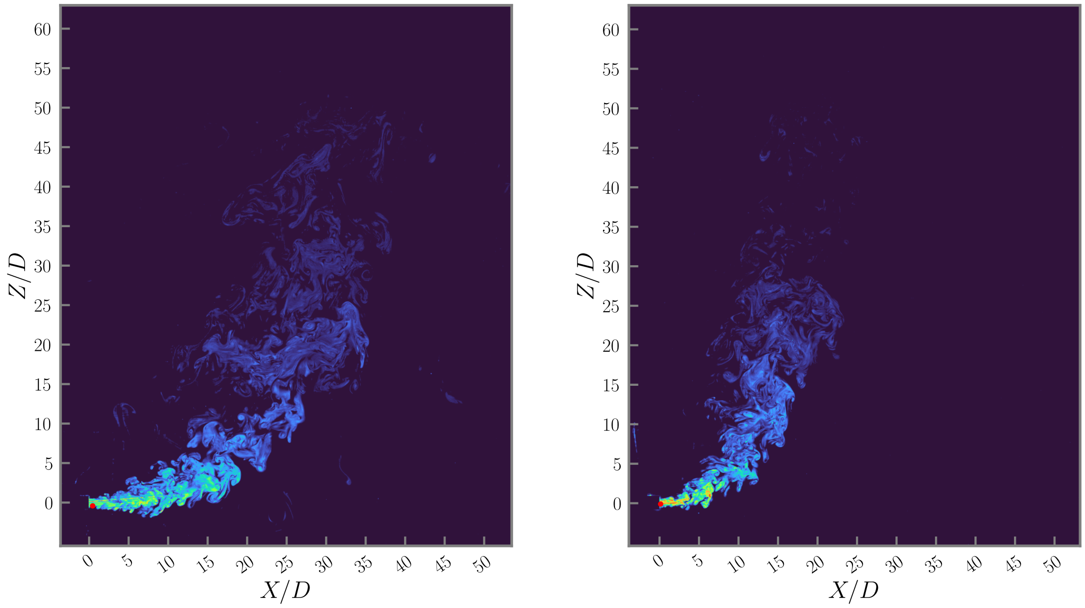

(a) (b)

Fig. 2.12 Normalized instantaneous concentration: (a) case 6, (b) case 22

$$R^2 = \left(\frac{\sum_{i=1}^{n} ((D - \overline{D}) \times (Y - \overline{Y}))}{\sqrt{\sum_{i=1}^{n} (D - \overline{D})^2 \times \sum_{i=1}^{n} (Y - \overline{Y})^2}} \right)^2 \tag{2.35}$$

$$NRMSE = \frac{RMSE}{\overline{Y}} \tag{2.36}$$

Where Y is the experimental value and D is the simulated value.

2.3.1 Model performance under different flow conditions

Comparing Case 6 and Case 22, it is evident that the prediction accuracy of x/D decreases in Case 22 for all turbulence models, as reflected by the increased NRMSE values presented in the concentration and trajectory comparisons. Among the governing dimensionless parameters, the Froude number is one of the most critical as it quantifies the relative dominance of inertial and buoyancy forces. A higher Froude number (typically $Fr > 4$) suggests a momentum-dominated regime with coherent jet development, whereas a lower Froude number ($Fr < 2$) corresponds to buoyancy-dominated conditions with enhanced flow complexity (Puggioni et al., 2025). As shown in Table 2.2, Case 6 exhibits a higher Froude number ($Fr = 5.81$) and jet velocity ($U_0 = 0.118$ m/s), indicating stronger inertial forces and a more stable and coherent jet.

Under these conditions, both the standard k-ε model and the RNG k-ε model can predict the centerline trajectory with high accuracy, especially the RNG k-ε model ($R^2=0.9763$, NRMSE=0.1506). The SST k-ω model shows a reasonably good correlation with the experimental trend ($R^2 = 0.9557$), but its higher RMSE value of 0.3223 suggests relatively large local deviations from the measured trajectory, indicating that its overall prediction accuracy is less satisfactory than the other two models.

However, in Case 22, the flow is more affected by buoyancy-induced instabilities due to the lower Froude number ($Fr = 2.23$) and lower Reynolds number ($Re = 558$) compared to Case 6 ($Re = 1111$). This results in a decrease in trajectory prediction for all models, especially the SST k-ω model, where the R^2 drops sharply to 0.6649 and the RMSE increases to 0.3922.

For centerline concentration prediction, the model's behavior is significantly different. In case 6, the RNG k-ε model achieves the best results ($R^2 = 0.9817$, RMSE = 0.0404), followed closely by the standard k-ε model. However, the SST k-ω model performs poorly in this case, with a relatively low R^2 of 0.7965 and a high RMSE of 0.2014, indicating that it cannot accurately resolve scalar transport under momentum-dominated conditions. Notably, this pattern is reversed in Case 22. The SST k-ω model achieves significantly better scalar prediction accuracy, with an R^2 increase of 0.9405 and a RMSE decrease of 0.0664, outperforming both k-ε-based models. This improvement shows that the SST formulation is better at capturing buoyancy-induced mixing and vertical entrainment in stratified flows. In contrast, the RNG k-ε model, while still maintaining a high R^2 (0.9492), has a significant increase in RMSE to 0.2014 in Case 22, underpredicting vertical mixing. The standard k-ε model maintains moderate accuracy in both cases, with relatively stable RMSE and R^2 values.

Overall, the performance of the models under different flow conditions reveals the sensitivity of RANS models to the dominant physical mechanisms. The SST k-ω model performs well only in terms of concentration behavior under high buoyancy conditions, the standard k-ε model provides consistent (but non-optimal) performance in both cases, and the RNG k-ε performs best overall, making it a reasonable choice for applications involving mixed flow properties.

2.3.2 Comparison of different turbulence models in trajectory prediction

To evaluate the prediction ability of different turbulence models for the centerline trajectory of the buoyancy jet, three turbulence models (standard k-ε, RNG k-ε and SST k-ω) were tested for two contrasting flow cases (Case 6 and Case 22) and compared with experimental measurements. The comparison was based on dimensionless trajectories (x/D vs. y/D) and evaluated using the squared Pearson correlation coefficient (R^2) and normalized root mean square error (NRMSE), and the results are summarized in Tables 2.4.

The origin of each trajectory was defined based on the nozzle exit centerline as observed in the images. In Figures 2.13 to 2.16, this corresponds to the point where the jet begins to visibly emerge. All coordinate axes (x=0, y=0) were aligned to this reference to ensure consistency in trajectory comparisons (Fischer, 1979).

Table 2.4 Accuracy comparison of predicted jet trajectories using different turbulence models.

Turbulence Model	Case	R^2	NRMSE
Standard k-ε	6	0.967654	0.162732
Standard k-ε	22	0.953097	0.170567
RNG k-ε	6	0.976309	0.150614
RNG k-ε	22	0.958683	0.154443
SST k-ω	6	0.955727	0.322311
SST k-ω	22	0.664923	0.392217

In both cases, the RNG k-ε model always maintains the highest prediction accuracy, with R^2 values exceeding 0.95 and the lowest NRMSE. In case 6, the Froude number is higher (Fr = 5.81), and the jet trajectory is dominated by momentum, causing the jet path to extend further laterally (as can be clearly seen in Figure 2.2(a)). This indicates that the momentum input is stronger, and the jet maintains a longer horizontal propulsion distance under the action of inertia. Under this condition, the RNG k-ε model accurately reproduces the experimental trajectory ($R^2 = 0.9763$, NRMSE = 0.1506), which is better than the standard k-ε model ($R^2 = 0.9677$, NRMSE = 0.1627) and the SST k-ω model ($R^2 = 0.9557$, NRMSE = 0.3223).

This agreement is clearly demonstrated in Figure 2.13(a), where the RNG and standard k-ε curves are relatively close to the experimental data, while the SST k-ω model slightly underestimates the lateral development. Figure 2.13(b) further confirms these results by comparing the simulated values to the measured values. Although the SST model exhibits relatively large local errors in Case 6 (as reflected in the higher NRMSE), its R^2 is still high as the overall trend is consistent with the experimental curvature. This acceptable performance can be attributed to the characteristics of Case 6, where the rosette-shaped buoyancy jet in a quiescent environment remains relatively coherent and is mainly affected by inertial forces.

In Case 22, the relatively low Froude number (Fr = 2.23) indicates that this region is dominated by buoyancy. Due to the reduced initial momentum, the jet is rapidly deflected upward in the vertical direction by buoyancy. Meanwhile, the limited lateral spread shown in Figure 2.12(b) reflects how buoyancy governs the plume evolution, promoting early upward movement and enhanced vertical mixing. This increases the complexity of accurately predicting the jet centerline. Nevertheless, the RNG k–ε model still maintains a strong correlation with the experimental results ($R^2 = 0.9587$, NRMSE = 0.1544), followed by the standard k–ε model ($R^2 = 0.9531$, NRMSE = 0.1706).

Figure 2.14(a) clearly illustrates this trend by comparing the predicted centerline trajectories of three turbulence models with experimental results. It also includes a reference curve from a single jet experiment (orange triangles), which shows a much greater horizontal displacement than the rosette jet under the same Froude number. This discrepancy can be attributed to the interaction between jets in the rosette configuration. In a single jet, the jet develops freely without interference from adjacent flows, allowing for larger entrainment and more extended trajectories. In contrast, the rosette-type discharge consists of closely spaced jets that interact with each other, reducing the effective entrainment area and suppressing lateral spreading. This suppression is particularly evident in Figure 2.14(a), where the experimental rosette trajectory (black circles) bends inward and rises faster than the single jet. The Coanda effect provides a physical explanation for this behavior: the mutual attraction of adjacent jets results in a lower-pressure region near the centerline, drawing the jets toward each other and further limiting their horizontal development. As stated by Yan et al. (2019), "the jet interactions restricted the jet spreading and ambient water entrainment, and the resultant low pressure near the centerline tended to attract the jets moving towards the low-pressure region". Saeidi Hosseini et al. (2022) also emphasized that such jet interactions significantly affect mixing characteristics, and that careful diffuser design is required to alleviate the adverse influence of the Coanda effect.

Figure 2.14(b) shows the SST k-ω predictions consistently falling below the identity line, indicating systematic underprediction of lateral displacement. The significant degradation in SST k-ω performance from Case 6 to Case 22 is likely due to its eddy-viscosity formulation being tuned for near-wall turbulence. It lacks curvature correction mechanisms and as a result, the model fails to capture the main features of the jet trajectory under buoyancy-dominated conditions.

These findings suggest that while all models perform well in high Fr number, momentum-dominated situations, only the RNG and standard k-ε models can effectively simulate trajectory curvature and enhance mixing at low Fr. In contrast, the SST k-ω model has limited reliability across scenarios, likely because its turbulence formulation is more suitable for near-wall flows than for buoyant jets. Therefore, the choice of turbulence model has a significant impact on trajectory predictions, especially when momentum and buoyancy balances change. As a result, the RNG k-ε model is the most robust and versatile of the three models tested for predicting the centerline trajectory of a rosette-shaped buoyant jet.

2.3.3 Comparison of different turbulence models in concentration prediction

To further evaluate the performance of the three turbulence models, the normalized centerline concentration distributions for Cases 6 and 22 were compared against experimental measurements. To ensure consistency and facilitate comparison across different scenarios, the vertical coordinate was non-dimensionalized as y/D, where D is the nozzle diameter. This non-dimensional form is widely adopted in jet flow studies as it eliminates the influence of absolute scale and enables a more general analysis of jet behavior across varying flow conditions and geometries.The predictions at different vertical positions (y/D) were assessed using the squared Pearson correlation coefficient (R^2) and normalized root mean square error (NRMSE), with the results summarized in Tables 2.5.

Table 2.5 Accuracy comparison of predicted normalized concentration using different turbulence models.

Turbulence Model	Case	R^2	NRMSE
Standard k-ε	6	0.944096	0.233000
Standard k-ε	22	0.957979	0.815720
RNG k-ε	6	0.981746	0.161578
RNG k-ε	22	0.949163	0.921312
SST k-ω	6	0.796486	0.567122
SST k-ω	22	0.940537	0.306554

In Case 6, all models capture the general trend of decreasing normalized concentration with increasing y/D. However, significant differences are observed in prediction accuracy. As shown in Figure 2.15(a), the RNG k-ε and standard k-ε models closely follow the experimental distribution, while the SST k-ω model significantly underpredicts concentration across the entire domain, particularly in the near field ($y/D < 10$). This is further illustrated in Figure 2.15(b), where the SST k-ω model's predictions fall well below the identity line, yielding the lowest correlation ($R^2 = 0.7965$) and the highest NRMSE (0.567122). By contrast, the RNG model achieves the highest agreement ($R^2 = 0.9817$, NRMSE = 0.1616), followed by the standard model ($R^2 = 0.9441$, NRMSE = 0.2330). The superior performance of the RNG k-ε model in this momentum-dominated regime may be attributed to its improved treatment of turbulent diffusion and shear-layer mixing, which dominated the scalar transport in the early stages of jet development.

In Case 22, the jet undergoes more rapid vertical deflection and dilution due to the dominance of buoyancy forces. As shown in Figure 2.16(a), all models predict a steeper concentration decay than in Case 6, which aligns with experimental observations. Notably, the SST k-ω model performs best in this scenario, exhibiting the lowest NRMSE (0.3066) and highest R^2 (0.9405), as shown in Figure 2.16(b). This improvement highlights the model's greater suitability for buoyancy-dominated flows, where vertical entrainment governs the scalar transport rather than momentum-driven shear. The standard k-ε model also maintains strong predictive performance ($R^2 = 0.9580$, NRMSE = 0.8157). In contrast, the RNG k-ε model, while still showing a high R^2 of 0.9492, tends to overpredict concentration in the mid-to-far field ($y/D > 15$), resulting in a higher NRMSE of 0.9213. This suggests that the RNG model underestimates the rate of vertical mixing under buoyant conditions.

These results indicate that the scalar prediction capabilities of turbulence models are strongly dependent on the flow regime. The RNG k-ε model performs best in high Fr, shear-dominated conditions but tends to underpredict vertical mixing when buoyancy dominates, leading to overconcentrated results. In contrast, the SST k-ω model, although less accurate in high-momentum flows, demonstrates better adaptability to buoyancy-driven jets.

However, this improved performance of the SST k-ω model in buoyant environments is limited to scalar fields and does not extend to trajectory prediction. As shown in Case 22, while the model achieves the lowest NRMSE in concentration, it performs poorly in reproducing the jet path ($R^2 = 0.6649$, NRMSE=0.3922). The standard k-ε model shows stable but average performance in predicting both the jet trajectory and the centerline concentration under different flow conditions.

This suggests that the choice of turbulence model should not only depend on whether the flow is momentum-dominated or buoyancy-dominated. It should also be considered what kind of results are needed depending on the operating parameters of the flow, whether the goal is to accurately simulate the trajectory of a jet or to predict how the concentration changes.

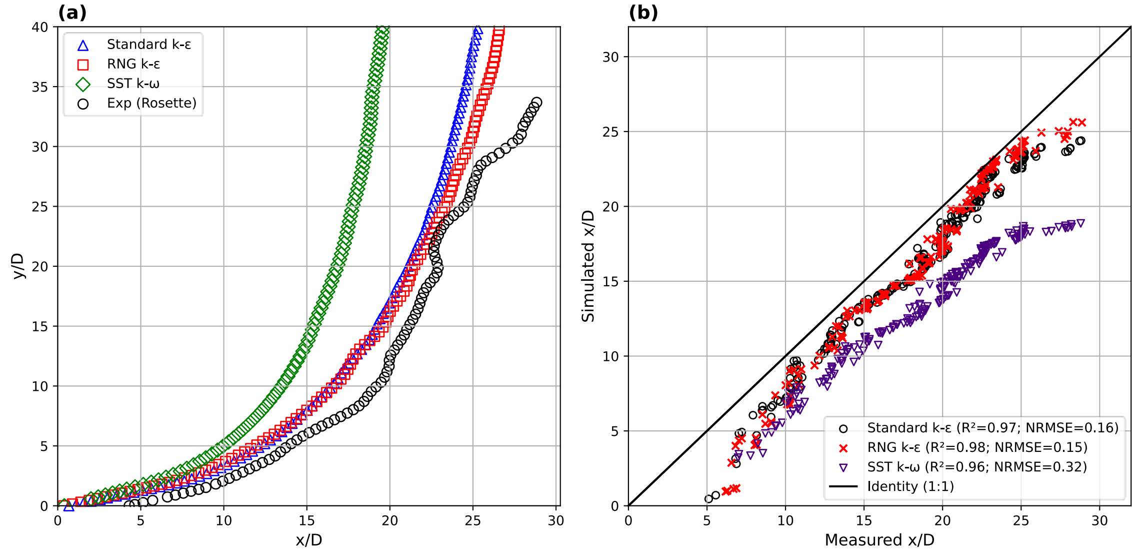

Fig. 2.13 Comparison of the experimental and numerical results of case 6. (a) x/D vs. y/D (b) measured x/D vs. simulated x/D.

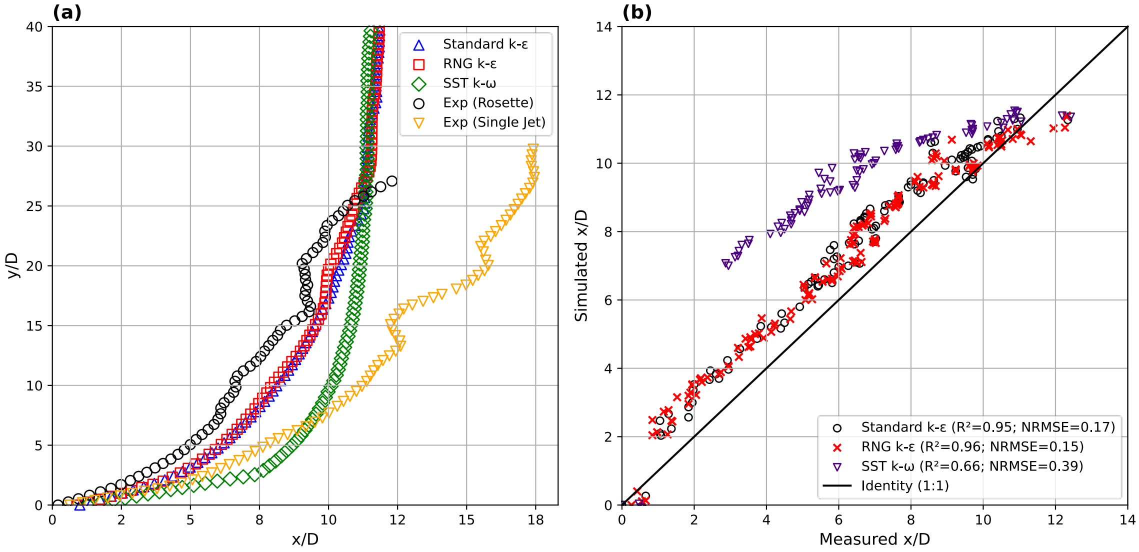

Fig. 2.14 Comparison of the experimental and numerical results of case 22. (a) x/D vs. y/D (b) measured x/D vs. simulated x/D.

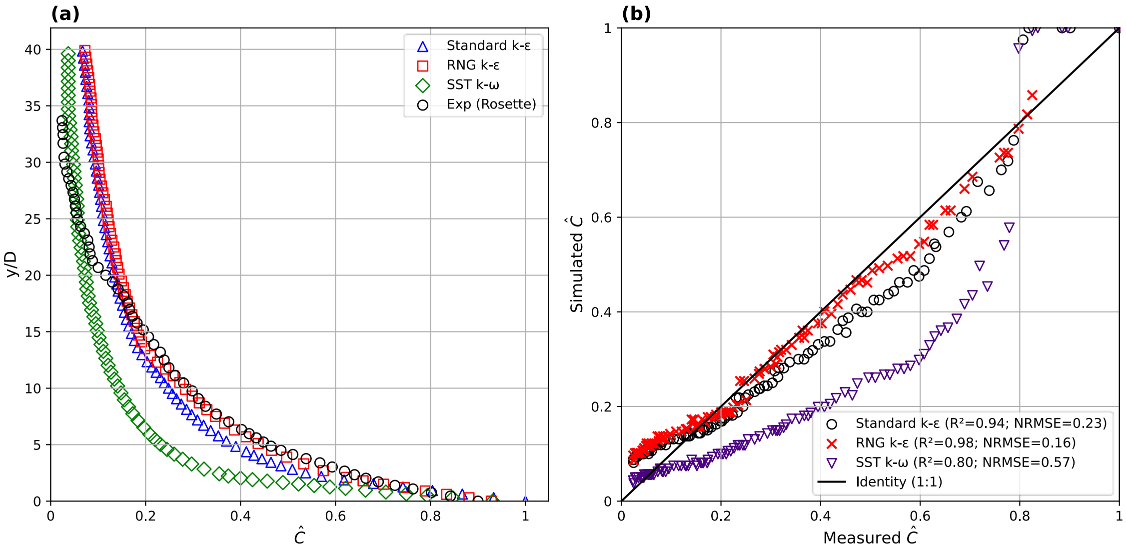

Fig. 2.15 Comparison of the experimental and numerical results of case 6. (a) normalized concentration vs. y/D (b) measured normalized concentration vs. simulated normalized concentration.

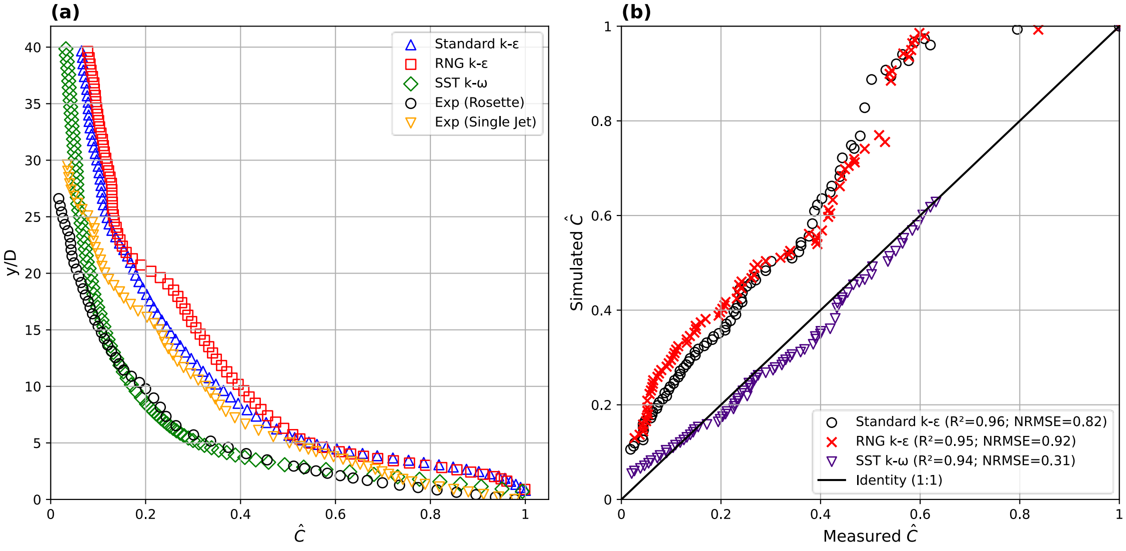

Fig. 2.16 Comparison of the experimental and numerical results of case 22. (a) normalized concentration vs. y/D (b) measured normalized concentration vs. simulated normalized concentration.

2.4 Conclusion

This chapter presents the results of a series of LIF experiments and compares the performance of three turbulence models - standard k-ε, RNG k-ε, and SST k-ω - in predicting rosette buoyancy jet trajectories and normalized concentrations under different flow conditions. The results show that the RNG k-ε model consistently provides the most accurate trajectory predictions, especially in the case of high Fr. The standard k-ε model shows stable but slightly less accurate performance in various cases. In contrast, the SST k-ω model has lower accuracy in trajectory predictions, especially in the case of low Fr numbers. However, for normalized concentration predictions, the SST model performs better at low Froude numbers, indicating its suitability for buoyancy-driven mixing. In summary, the results emphasize that turbulence model performance is sensitive to the flow regime and that no single model is universally optimal. Therefore, the choice of turbulence model should consider the dominant flow regime and the specific prediction objectives.

Chapter III Application of Machine Learning in Simulation of Buoyant Rosette Jet

3.1 Introduction and literature review

This study presents a hybrid framework for modeling the concentration distribution of rosette-type multiport buoyant jets commonly used in wastewater discharge systems. To address the limitations of conventional methods such as the high cost of physical experiments and the computational demand of CFD simulations a combined experimental, , and machine learning (ML) approach is employed. High-resolution scalar concentration fields were obtained through Laser-Induced Fluorescence (LIF) experiments conducted under varying hydraulic conditions. These datasets were subsequently used to train three data-driven models: Extreme Learning Machine (ELM), Adaptive Neuro-Fuzzy Inference System (ANFIS), and Multivariate Adaptive Regression Splines (MARS). The models were tested for their ability to predict jet trajectory, centerline dilution, and mixing length. Comparative results demonstrate that ML algorithms can achieve reliable predictions at a fraction of the computational cost, offering rapid tools for environmental modeling. The study provides practical insights into model selection for real-time assessment and optimization of diffuser system performance.

3.1.1 Introduction

The diffusion behavior of rosette-type multiport buoyant jets is characterized by intricate, hybrid dynamics resulting from the simultaneous influence of turbulent entrainment, buoyancy-driven rise, and the mutual interaction of closely spaced individual jets. These complex flow features are especially relevant in environmental engineering applications such as wastewater discharge into receiving water bodies, where accurate modeling of dilution and mixing processes is essential for assessing environmental impact and optimizing diffuser design.

High accuracy experimental methods such as Laser-Induced Fluorescence (LIF) for concentration fields and Particle Image Velocimetry (PIV) for velocity measurements have been extensively used to investigate these jets. These techniques offer high spatial and temporal resolution, enabling detailed characterization of centerline dilution, merging behavior, and mixing zones. However, they also come with substantial drawbacks, including the need for sophisticated instrumentation, high operating costs, and significant time and labor investments.

In parallel, Computational Fluid Dynamics (CFD) has become a widely used tool for analyzing jet behavior under various hydraulic and geometric configurations. CFD enables full-field predictions and parametric testing but is often hindered by long simulation times, sensitivity to mesh and turbulence model selection, and the high computational resources required for simulating multiple scenarios or real-time conditions.

To overcome these limitations, this study proposes a hybrid modeling strategy that combines experimental accuracy with the computational efficiency of machine learning (ML). A series of LIF experiments were performed under varied hydraulic conditions—including multiple Froude numbers, nozzle spacings, and flow rates to generate a robust dataset of scalar concentration fields. . The machine learning component focuses on three techniques: Extreme Learning Machine (ELM), known for its high-speed learning and minimal tuning requirements; Adaptive Neuro-Fuzzy Inference System (ANFIS), which blends fuzzy logic with neural learning to model uncertainty and nonlinear behaviors; and Multivariate Adaptive Regression Splines (MARS), which builds flexible, interpretable models through piecewise regression and interaction terms.

The study's core objective is to evaluate each model's ability to predict key jet behavior metrics such as centerline dilution, mixing length, and trajectory shape with high accuracy and reduced computational effort. Finally, a comparative analysis was performed to identify the strengths, limitations, and practical applicability of each ML model.

This investigation contributes to the growing body of research integrating data-driven techniques into environmental hydraulics. It demonstrates that well-trained ML models, supported by high-fidelity experimental datasets, can significantly reduce reliance on expensive simulations while preserving predictive accuracy. The results advocate for broader adoption of hybrid approaches in diffuser design, outfall impact prediction, and real-time water quality management systems.

3.1.2 Literature review

Traditional studies of buoyant jets, such as those by Roberts (1979) and Jirka (2004), have established fundamental insights into jet behavior, including dilution rates and plume trajectories. However, they are exposed to experimental limitations.

The integration of machine learning (ML) with fluid dynamics has gained momentum as a means to overcome these limitations. Early studies focused on surrogate models (Forrester et al., 2008) and order reduction techniques (Brunton et al., 2020), demonstrating the potential of ML to accelerate simulations while maintaining accuracy. For example, Duraisamy et al. (2019) applied neural networks to turbulence modeling, significantly reducing computational time.

In recent years, some specific ML algorithms have shown promise in related areas: Huang et al. (2006) highlighted the effectiveness of the Extreme Learning Machine (ELM) in hydrological modeling, thanks to its single hidden layer architecture and fast training. Jang (1993) pioneered the application of ANFIS to environmental systems, where fuzzy logic enhanced the interpretability of noisy datasets. Friedman (1991) demonstrated the advantages of MARS in handling nonlinear engineering problems through piecewise linear approximation. The integration of machine learning (ML) models with experimental and numerical methods has gained increasing interest in the simulation of hydraulic and environmental systems. Among various models, Extreme Learning Machine (ELM), Adaptive Neuro-Fuzzy Inference System (ANFIS), and Multivariate Adaptive Regression Splines (MARS) have demonstrated notable success in modeling nonlinear processes related to fluid flow, sediment transport, and mixing phenomena. These models are particularly useful for approximating complex relationships in environmental datasets where traditional approaches may be limited by computational cost or a lack of comprehensive physical understanding.

ELM is a single-layer feedforward neural network known for its extremely fast training speed and excellent generalization ability. It eliminates the need for iterative parameter tuning by randomly assigning input weights and analytically determining output weights. This feature makes ELM especially suitable for real-time or large-scale environmental modeling tasks. In hydraulic engineering, Ebtehaj et al. (2018) developed an ELM-based framework for predicting scour at pile groups under clear water conditions. Ebtehaj et al. (2016) demonstrated its effectiveness in estimating sediment transport, while further work by the same research group (Ebtehaj et al., 2019) applied ELM to forecast scour depth around bridge piers with high accuracy. Bonakdari et al. (2020) showed that ELM could successfully model complex velocity fields in narrow open channels. ELM has also been used for sensitivity analysis of hydraulic parameters (Azimi et al., 2017a), stream health evaluation (Aredah et al., 2022), and to predict flow variables in curved irrigation channels (Bonakdari et al., 2021). Merabet and Heddam (2023) compared ELM with other machine learning techniques and highlighted its effectiveness in environmental modeling, particularly for complex, high-dimensional datasets.

ANFIS integrates the interpretability of fuzzy logic with the learning capabilities of neural networks. Its rule-based structure allows for the modeling of uncertainty and imprecision in data, which is common in hydraulic systems. ANFIS has been used in numerous hybrid configurations, often in conjunction with optimization algorithms such as genetic algorithms (GA), particle swarm optimization (PSO), and firefly algorithm (FA). Gholami et al. (2018) employed a GA-PSO-ANFIS model to predict the threshold bank profile shape of stable channels using laser scanning techniques. Similarly, Azimi et al. (2017b) applied Pareto-based evolutionary optimization to enhance the prediction accuracy of ANFIS in modeling scour development at pile groups. Azimi et al. (2018) demonstrated that ANFIS, when combined with FA, can effectively predict the roller length of hydraulic jumps on rough channel beds. These examples reflect ANFIS's adaptability and robustness in handling multi-variable, nonlinear hydraulic problems. The application of ANFIS in environmental and hydrological modeling has proven highly effective in previous studies. For instance, Masroor et al. (2023) applied ANFIS to assess drought vulnerability in the Godavari sub-basin and reported high predictive performance with Receiver Operating Characteristic – Area Under the Curve (ROC-AUC) scores exceeding 0.95 in short- and long-term drought scenarios. Similarly, Jasmine (2020) demonstrated that ANFIS can outperform other AI models in evaporation estimation tasks due to its simplicity, adaptability, and ability to incorporate fuzzy reasoning, making it a robust option for hydrological applications.

MARS is a flexible nonparametric regression technique that constructs piecewise linear basis functions to model nonlinearities and interactions in the data. Unlike traditional regression models, MARS automatically selects relevant variables and their interactions, making it ideal for high-dimensional problems with limited prior knowledge. Although its application in hydraulic engineering is relatively less common, its strengths have been highlighted in specific contexts. Nayeem et al. (2025) used MARS to analyze the colorization process during lactulose production, offering insights into nonlinear physicochemical interactions. Shaghaghi et al. (2019) applied MARS, along with M5 model trees and support vector regression, to predict the geometry of regime rivers based on field and morphological parameters, highlighting its utility in morphological analysis and water resources engineering. Tao et al. (2021) provided a comprehensive overview of MARS in hydrological modeling, emphasizing its role in sediment transport prediction and highlighting its advantages in model interpretability and adaptability.

In the study of rosette type multiport jets, Yan and Mohammadian (2020) first combined multi-gene genetic programming (MGGP) with computational fluid dynamics (CFD) to predict the mixing characteristics of dense jet groups under crossflow conditions, including terminal rise height, impact distance, and impact dilution. Experimental data were used for model training and validation. The results showed that the MGGP-based model outperformed the traditional empirical formula in terms of accuracy and interpretability, providing strong scalability and real-time applicability for practical diffuser design. Subsequently, Yan et al. (2021) extended the MGGP-CFD method to simulate the buoyant discharge of rosette type diffusers. The method significantly reduced the computational time while maintaining prediction accuracy, further confirming the potential of MGGP for efficient modeling. However, the inherent complexity and susceptibility to overfitting of MGGP highlight the need for comparative studies with other machine learning (ML) techniques. However, the inherent complexity and susceptibility to overfitting of MGGP highlight the need for comparative studies with other machine learning (ML) techniques. To this end, Yan et al. (2022) developed a hybrid CFD-convolutional neural network (CNN) model to simulate the concentration field of multiport buoyant jets, especially for rosette diffusers. The model uses OpenFOAM to generate an extended CFD dataset for CNN training and prediction. Compared with the MGGP model, the CFD-CNN model significantly improves computational efficiency while maintaining high accuracy, demonstrating its excellent ability to process high-dimensional spatial data, marking the first application of CNN in three-dimensional buoyant jet simulation.

Collectively, these studies underscore the potential of ELM, ANFIS, MARS, or other ML models as powerful tools for modeling hydraulic and environmental phenomena. Their capacity for capturing nonlinear relationships, handling large and noisy datasets, and producing interpretable or efficient models make them strong candidates for simulating the mixing behavior and concentration fields of buoyant rosette jets. Despite these advances, some gaps remain, with most studies focusing on a single machine learning algorithm and lacking comparative evaluations of ELM, ANFIS, and MARS.

Rosette jet simulations require explicit modeling of multi-source interactions, while existing alternative models are often oversimplified. The trade-off between model interpretability and computational efficiency has not been fully explored in the laboratory experiment-machine learning hybrid framework.

This study addresses these deficiencies by rigorously testing the capabilities of ELM, ANFIS, and MARS in predicting rosette jet concentration fields, trained using laboratory experimental data. Integrating these machine learning models with experimental data, such as those obtained through laser-induced fluorescence (LIF) techniques, offers a promising pathway to enhance accuracy and reduce computational demands in CFD-based environmental flow analysis.

3.2 Methodology

There are three important basic links in applying machine learning (ML) technology to simulate buoyant rosette type jets: data generation, model development, and performance verification, as shown in Figure 3.1. Among them, data generation is to obtain high-fidelity training and test data sets from laboratory experiments or numerical simulations (in this study, all the data used are from laboratory experiments), and pre-processing of parameters (including inputs and targets) such as normalization. Ensure that the jet dynamics under various flow conditions are fully covered. Model development includes selecting a suitable ML algorithm, training a regression model to capture the nonlinear relationship between jet parameters and concentration field, and adjusting model parameters to improve the optimization accuracy and generalization ability of the model. Finally, model verification includes using an independent test data set to evaluate the predictive ability of the trained model through statistical indicators (such as R^2, MAE and RMSE) and visual analysis (such as sample sequence comparison and scatter plots), thereby verifying its applicability in predicting jet behavior under unknown conditions.

3.2.1 Data generation and preprocessing

This dataset is generated by extracting the experimental average concentration images of 34 different Fr through a Python code, and the input parameters include Fr, x/D, y/D and normalized concentration. Among them, the mean, minimum, maximum, median, standard deviation, variance, kurtosis and skewness of Fr are 2.937, 0.417, 5.810, 2.905, 1.488, 2.213, -0.702, and 0.276 respectively. The mean, minimum, maximum, median, standard deviation, variance, kurtosis and skewness of x/D are 17.19, 3.353, 32.971, 16.944, 6.034, 36.405, -0.558, and -0.005 respectively. The average, minimum, maximum, median, standard deviation, variance, kurtosis, and skewness of the normalized concentration are 0.693, 0.234, 1.000, 0.698, 0.190, 0.036, -0.927, and -0.172, respectively. The average, minimum, maximum, median, standard deviation, variance, kurtosis, and skewness of y/D are 18.84, 15.000, 23.000, 19.000, 2.358, 5.561, -1.166, and 0.044, respectively.

The y/D value in Chapter 2 starts from 0, which is different from the experiments and CFD research in Chapter 2. The y/D value of the dataset used in machine learning starts from 15. This is because in the LIF experiment, the concentration data in the area lower than the nozzle will be blocked, which is an inevitable experimental limitation in the experimental process. This exclusion is attributed to limitations in the LIF experimental technique, where laser shadowing near the nozzle obstructs optical access, leading to inevitable experimental uncertainty in concentration measurements.

In this chapter, a large region was selected to obtain more accurate machine learning simulation results. The main purpose is to compare the prediction performance of different models. The final data set contains four parameters: Fr, x/D, y/D and normalized concentration, where Fr, x/D, y/D are inputs and normalized concentration is output, with a total of 870 data points. The final dataset has a total of 870 data points. In machine learning, these data points are randomly divided into training and test sets, of which 70% are used for model training and 30% are used for testing. This division is intended to ensure an objective evaluation of the predictive performance of the machine learning model.

3.2.2 Model development

Extreme learning machine (ELM), adaptive neuro-fuzzy inference system (ANFIS), and multivariate adaptive regression splines (MARS) were employed as machine learning models for predicting the normalized concentration field of buoyant rosette type jets. As described in sections 3.1.1 and 3.1.2, these models have been widely applied in environmental modeling due to their ability to capture complex nonlinear relationships. Among them, ANFIS benefits from a hybrid learning mechanism that combines the interpretability of fuzzy systems with the learning capability of neural networks, while ELM offers fast training and strong generalization performance, and MARS provides interpretable, piecewise-linear models with automatic variable selection. All of this study used MATLAB for model training and evaluation of training and test data.

Figure 3.1 shows a schematic diagram of the ANFIS model structure, which shows a five-layer structure. Each input will go through the fuzzification, rule application, normalization， defuzzification and aggregation layers to ultimately produce a valid output, which in this study represents the predicted normalized concentration. This multi-layer structural design enables ANFIS to effectively model nonlinear systems while maintaining interpretability.

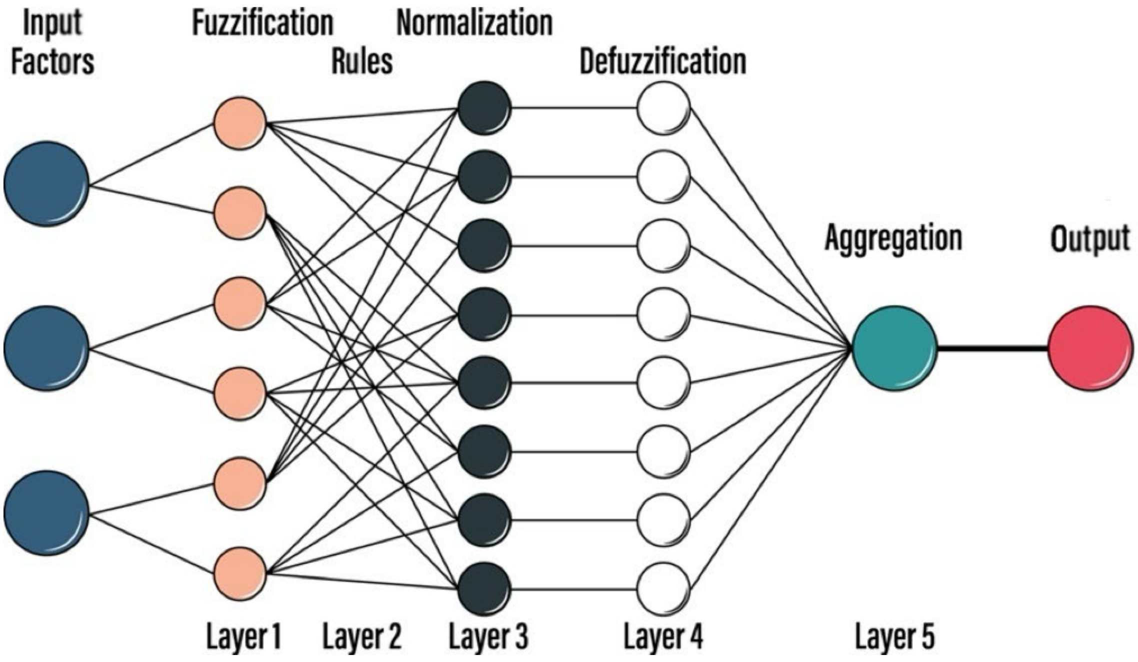

Fig. 3.1 The schematic structure of ANFIS model (Masroor et al., 2023).

The ELM model consists of an input layer, a single hidden layer, and an output layer (as shown in Figure 3.2). Among them, the input weights and biases connecting the input layer and the hidden layer are randomly assigned and fixed, and the output weights are calculated analytically using the Moore-Penrose generalized inverse. This structure gives ELM a fast training speed and good generalization performance, making it suitable for high-dimensional regression tasks (Huang et al., 2015; Merabet & Heddam, 2023).

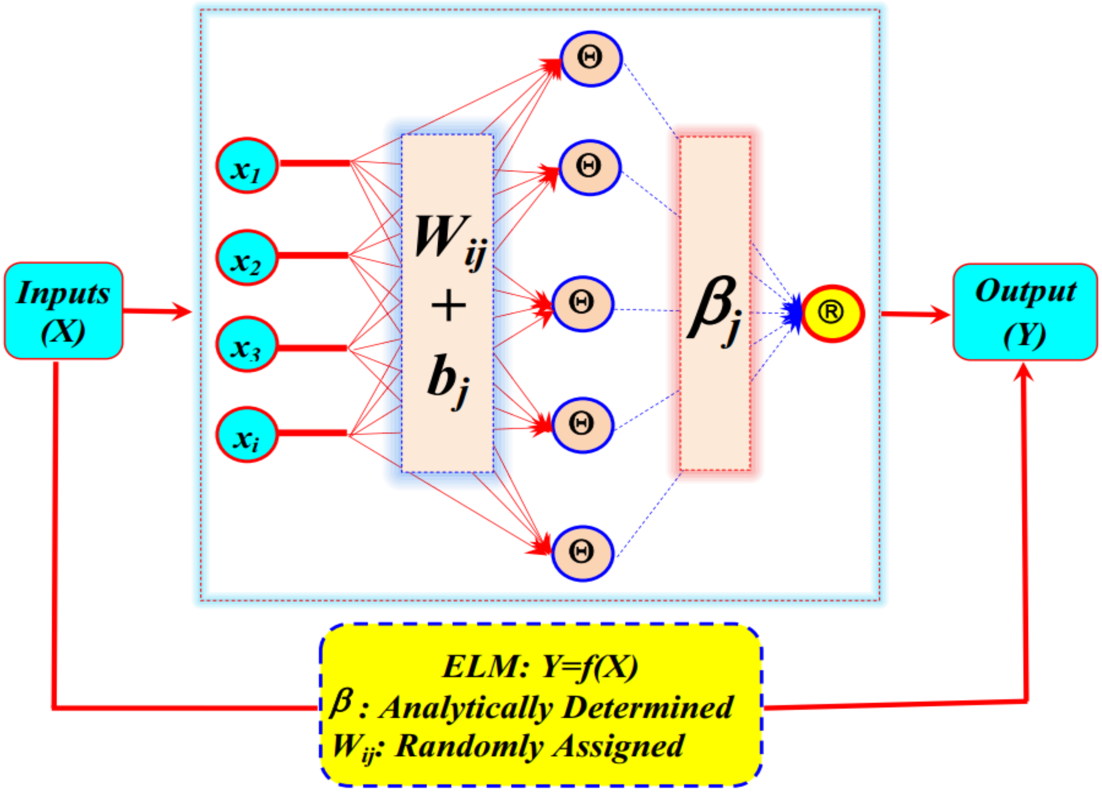

Fig. 3.2 The schematic structure of ELM model (Merabet & Heddam, 2023).

Figure 3.3 shows the architecture of the multivariate adaptive regression spline (MARS) model used in this study. The model constructs a series of basis functions (BFs) through forward selection and backward elimination processes. The forward phase adds functions to improve fitness, while the backward phase removes terms that cause overfitting. Each BF corresponds to a piecewise linear function defined by a node, which enables the MARS model to capture nonlinearities and interactions between input variables, and a series of formulas are obtained to predict the output (which will be shown in the next section). This flexible and data-driven approach enables MARS to model complex relationships in environmental data adaptively.

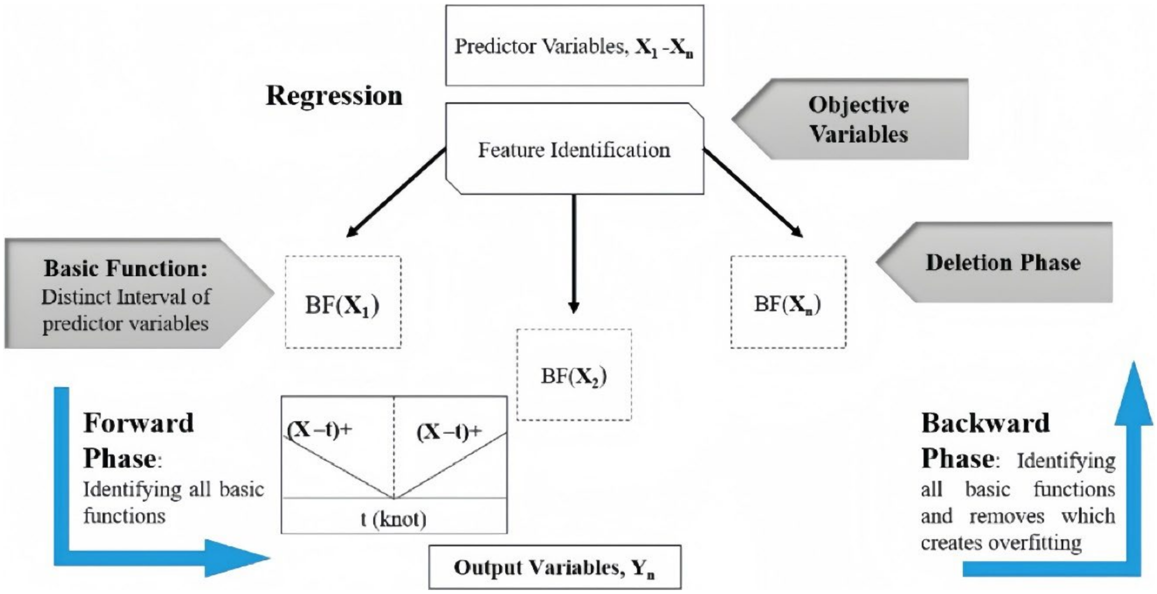

Fig. 3.3 The schematic structure of MARS model (Tao et al., 2021).

3.3 Result and discussion

The performance of the ANFIS, MARS, and ELM models in predicting the normalized concentration is shown in Figures 3.4–3.6. Each figure provides a qualitative and quantitative evaluation of the model predictions through (a) sample sequence comparison and error analysis of the training dataset; (b) sample sequence comparison and error analysis of the test dataset; (c) scatter plot of experimental values vs. predicted values of the training dataset and (d) scatter plot of experimental values vs. predicted values of the test dataset. In order to be able to directly and objectively compare the prediction accuracy of the models, statistical indicators such as the coefficient of determination (R²), mean absolute error (MAE), and root mean square error (RMSE) were calculated (defined by eq. 3.1-3.3). The detailed values of these indicators are summarized in Tables 3.1 and 3.2, corresponding to the training and test datasets, respectively. These indicators provide a comprehensive basis for evaluating the relative performance and generalization ability of each model.

$$R^2 = \left(\frac{\sum_{i=1}^{n} (D_i - \overline{D})(Y_i - \overline{Y})}{\sqrt{\sum_{i=1}^{n} (D_i - \overline{D})^2} \cdot \sqrt{\sum_{n-1}^{n} (Y_i - \overline{Y})^2}} \right)^2 \qquad (3.1)$$

$$MAE = \frac{1}{n}\sum_{i=1}^{n}\left|D_i - Y_i\right| \tag{3.2}$$

$$RMSE = \sqrt{\frac{1}{n}\sum_{n-1}^{n}(D_i - Y_i)^2} \tag{3.3}$$

where D_i is simulated value, Y_i is measured value, $\overline{D}$ is the mean of simulated value and $\overline{Y}$ is the mean of measured value.

Table 3.1 Model performance on training dataset.

Model	R^2	MAE	RMSE
ANFIS	0.9704	0.0235	0.0332
MARS	0.7109	0.0786	0.1041
ELM	0.8317	0.0578	0.0780

Table 3.2 Model performance on testing dataset.

Model	R^2	MAE	RMSE
ANFIS	0.9088	0.0376	0.0551
MARS	0.6629	0.0764	0.1049
ELM	0.8343	0.0578	0.0771

The performance of the ANFIS model in predicting the normalized concentration field is shown in Figure 3.4. Sub-figures (a) and (b) show the time series comparison of the measured and predicted values for the training and test datasets, respectively, as well as the corresponding prediction errors and error distributions. In both datasets, the predicted concentrations are very consistent with the measured values. The errors fluctuate slightly around zero and are approximately normally distributed, with no obvious trends or systematic deviations.

The scatter plots in Figures (c) and (d) further confirm the prediction accuracy of the model. In the training data, the predicted values closely match the diagonal line representing perfect agreement, indicating high correlation and small residuals. Tables 3.1 and 3.2 show that the coefficient of determination $R^2 = 0.9704$ and the error indicators MAE = 0.0235 and RMSE = 0.0332 for the training dataset. For the test data, the ANFIS model still maintains a high prediction performance, with a determination coefficient $R^2 = 0.9088$, error index MAE = 0.0376, and RMSE = 0.0551, all of which are better than MARS and ELM.

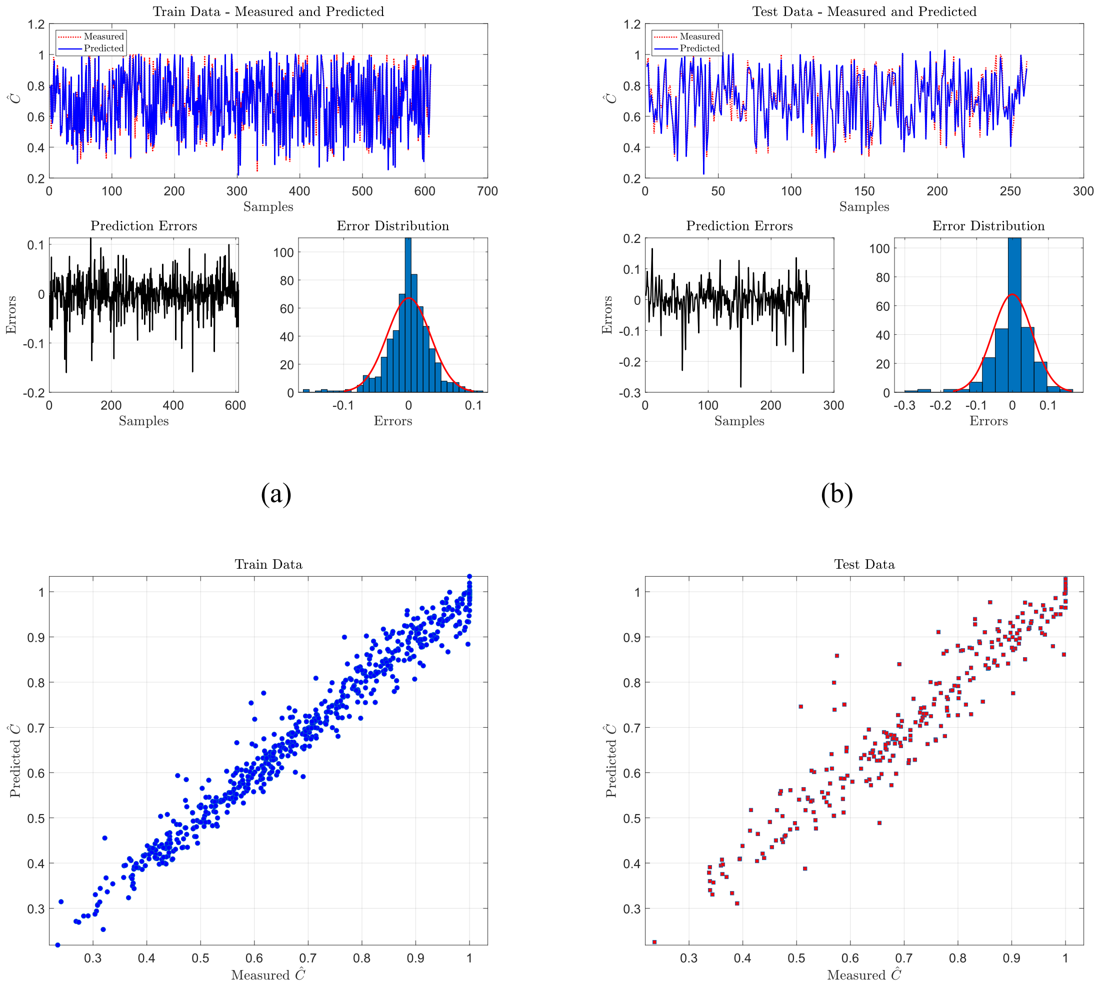

(a) (b)

(c) (d)

Fig. 3.4 ANFIS model performance in predicting normalized concentration fields: comparison of actual and predicted values: (a) training data: error analysis (b) testing data: error analysis (c) training data: predicted vs.

actual scatter plot (d) testing data: predicted vs. actual scatter plot.

These results show that the ANFIS model has strong generalization ability and can accurately capture the nonlinear relationship between input features (Fr, x/D, y/D) and normalized concentration. The hierarchical structure of ANFIS combines fuzzy logic with data-driven learning, which can perform robust reasoning even in the presence of local discontinuities or sharp turbulence in the concentration field. This hybrid structure enhances interpretability while retaining approximation capabilities, making ANFIS suitable for modeling complex environmental transport phenomena.

Figure 3.5 shows the performance of the MARS model in predicting the normalized concentration. As shown in sub-figures (a) and (b), comparing the measured and predicted values in the training and test datasets shows that the model captures the general trend of the data, although there are still obvious fluctuations. The error plot shows that the residuals are centered at zero, while the error distribution histogram shows an approximately normal distribution, which means that the prediction results are not significantly biased.

Sub-figures (c) and (d) show the scatter plots of the measured and predicted values in the training and test datasets, respectively. During the training phase, the predicted values show a fairly strong correlation with the measured values, but there is obvious discreteness at lower concentration levels. During the testing phase, this discreteness becomes more obvious, especially in the low and medium concentration ranges, indicating that the generalization ability of the model has decreased in these regions. This observation is consistent with the low R^2 value of 0.6629 and the relatively high RMSE of 0.1049 (Table 3.2), which reflects the limitations of the model's predictive ability.

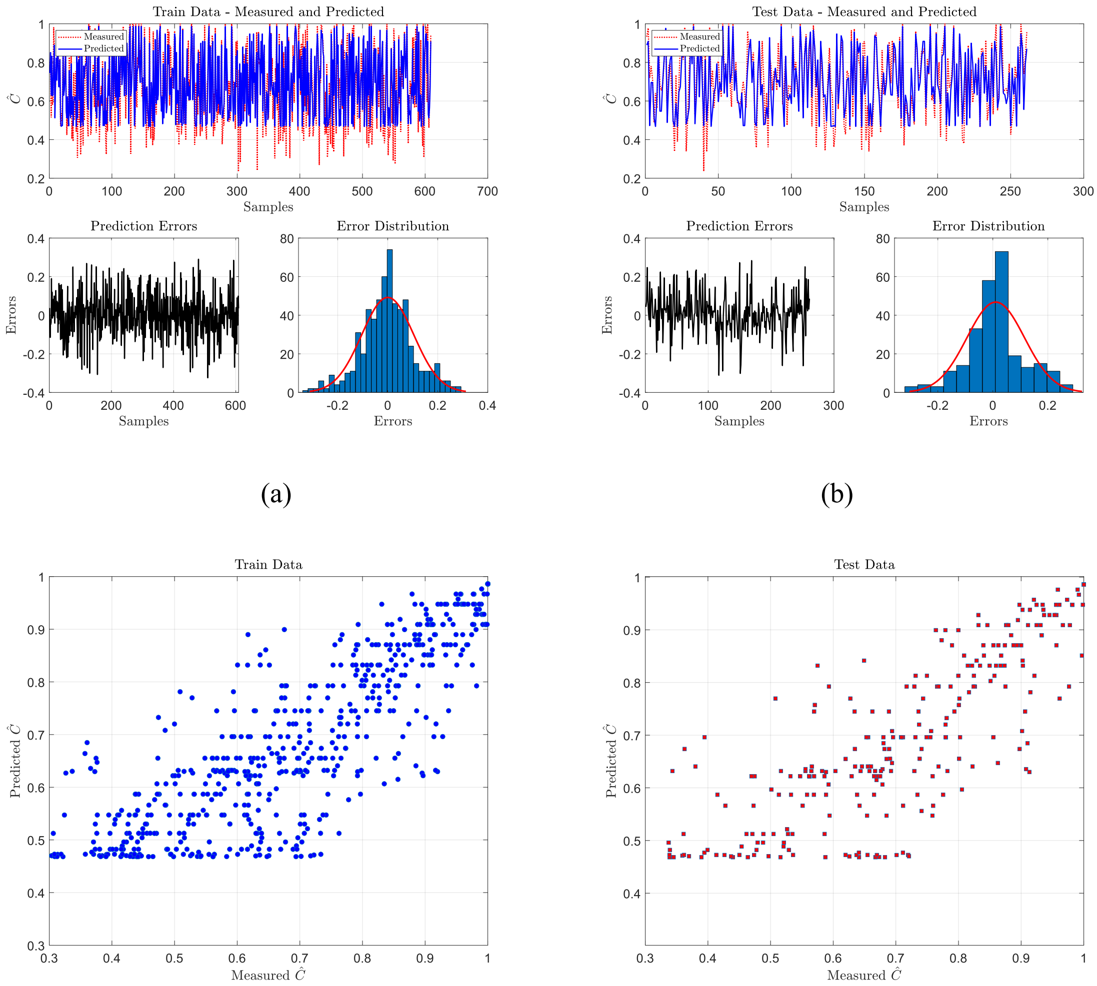

(a) (b)

(c) (d)

Fig. 3.5 MARS model performance in predicting normalized concentration: comparison of actual and predicted values: (a) training data: error analysis (b) testing data: error analysis (c) training data: predicted vs. actual scatter plot (d) testing data: predicted vs. actual scatter plot.

However, the MARS model gives three basis functions based on a single input variable x_3 (i.e., y/D in this study), adopts a continuous and interpretable piecewise linear structure, and can flexibly capture the nonlinear relationship between input and output. The resulting prediction expression is as follows:

$$BF_1 = \max(0,\ 19.625 - x_3) \tag{3.4}$$

$$BF_2 = \max(0,\ 19.75 - x_3) \tag{3.5}$$

$$BF_3 = \max(0,\ x_3 - 19.5) \tag{3.6}$$

$$\widehat{C} = 0.6156 + 0.1929 \cdot BF_1 - 0.1083 \cdot BF_2 - 0.0478 \cdot BF_3 \tag{3.7}$$

Where $\widehat{C}$ is predicted normalized concentration is, x_3 is input variables, corresponding to y/D, BF_i is piecewise basis function, used for local modeling, $\max(0,\ c \pm x)$ is hinge function, which takes effect at a specific breakpoint (knot) to form a nonlinear turning point of the model, 0.1929, −0.1083, −0.0478 are coefficients, indicating the weighted influence of the corresponding basis function on the output.

When $x_3 < 19.5$: BF_1 and BF_2 are effective, BF_3 is zero; when $19.5 \le x_3 \le 19.75$: all basis functions may be effective at the same time; when $x_3 > 19.75$: all BF are 0, and the output is always a constant of 0.6156.

Although the MARS model is interpretable and performs well on the training dataset, it shows decreased accuracy and limited generalization ability on the test dataset, making it difficult to accurately predict changes in the concentration field. This may be due to the model's reliance on a single input variable and a limited number of basis functions, which limits its ability to capture multivariate interactions, and complex nonlinearities present in the system.

Figure 3.6 displays the predictive performance of the ELM model on the normalized concentration field. As shown in subfigures (a) and (b), the model captures the fluctuation trends of the measured values in both the training and testing datasets, with reasonably aligned predicted curves. The error plots indicate relatively narrow fluctuations around zero, and the error histograms follow an approximately Gaussian distribution, implying an overall unbiased prediction tendency.

The scatter plots in subfigures (c) and (d) further validate the predictive accuracy of the ELM model. In the training dataset, the predicted values show a tight clustering along the 1:1 reference line, indicating good agreement between predicted and measured normalized concentrations. The corresponding performance metrics — R^2=0.8317, MAE = 0.0578, RMSE = 0.0780 — suggest that ELM can effectively approximate the training data with moderate accuracy.

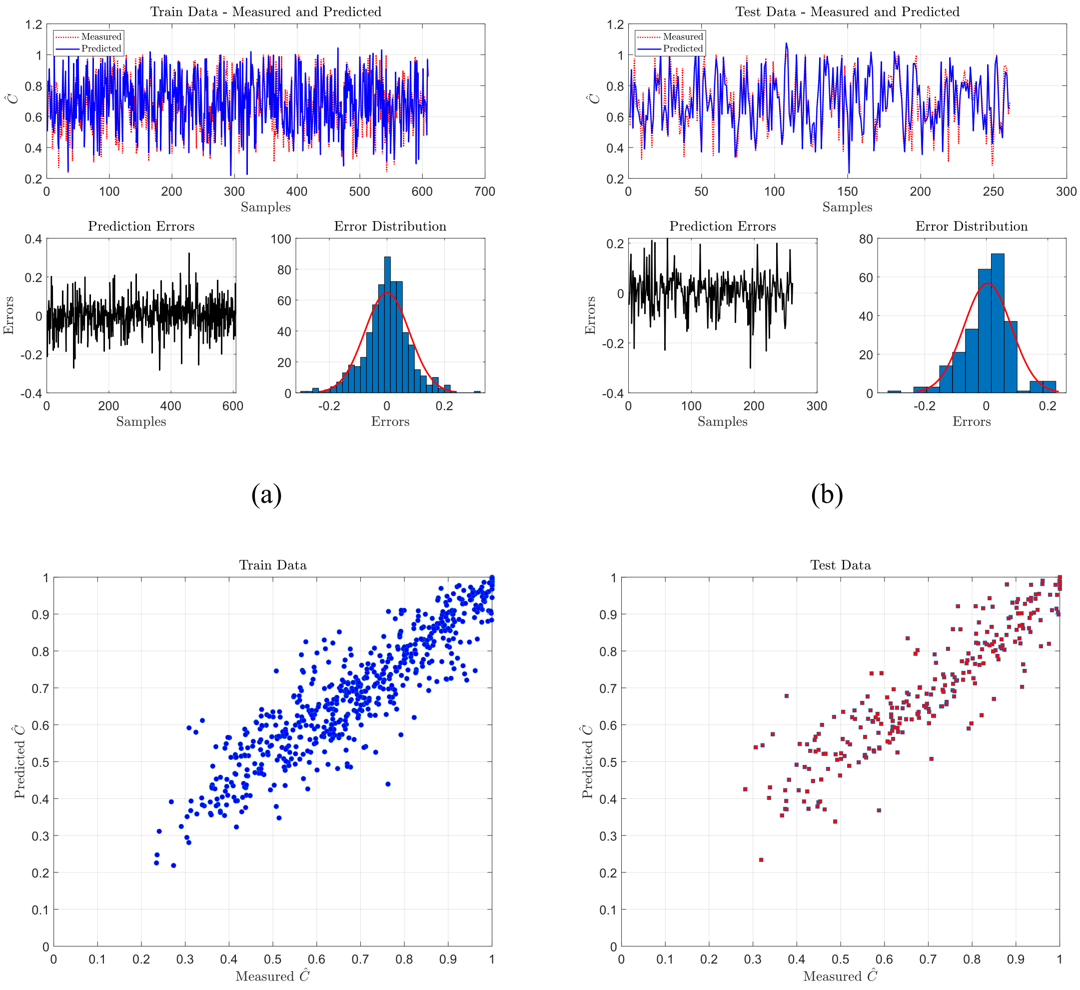

(a) (b)

(c) (d)

Fig. 3.6 ELM model performance in predicting normalized concentration fields: comparison of actual and predicted values: (a) training data: error analysis (b) testing data: error analysis (c) training data: predicted vs. actual scatter plot (d) testing data: predicted vs. actual scatter plot.

In the testing dataset, the model maintains decent generalization ability, achieving an R^2 of 0.8343, MAE = 0.0578, and RMSE = 0.0771 (Table 3.2). Although the accuracy is lower than ANFIS, it is noticeably better than that of the MARS model. The scatter plot reveals that while the ELM model performs well in high-concentration regions, there is more dispersion in mid-range values, indicating localized underfitting or sensitivity to input variability.

The performance of ELM can be attributed to its architecture, in which the input weights and biases are randomly generated and fixed, and the output weights are analytically determined using the Moore–Penrose pseudoinverse. This structure can achieve extremely fast training speed and reduce the risk of overfitting. However, its reliance on random initialization may limit the model's ability to capture complex nonlinear patterns in specific areas. Even though ELM is not the best choice, it strikes a good balance between training efficiency and prediction accuracy, making it a practical choice for real-time or large-scale environmental prediction tasks.

3.4 Conclusion

In this chapter, three machine learning models, namely adaptive neuro-fuzzy inference system (ANFIS), extreme learning machine (ELM) and multivariate adaptive regression spline function (MARS), are comprehensively studied for the prediction of normalized concentration field of buoyancy rose-shaped multi-port jets, and their prediction capabilities are quantitatively evaluated using determination coefficients and error indicators. These models are trained and tested using experimental data obtained through laser-induced fluorescence (LIF) technology experiments, thus realizing a data-driven modeling approach that is different from traditional laboratory experiments or CFD simulations.

The prediction results showed that all three models can capture the nonlinear relationship between jet parameters (Fr, x/D, y/D) and normalized concentration to varying degrees. Among them, the ANFIS model significantly outperforms the other two models in both training and testing stages, with the highest determination coefficient ($R^2 = 0.9704$ in the training stage and $R^2 = 0.9088$ in the testing stage) and the lowest error indicator. Its hybrid structure combines fuzzy reasoning and neural network learning, effectively generalizing and generating robust predictions even under unknown conditions. This may be attributed to its simple model development, easy operation, ability to handle heterogeneous indicators and reduce statistical restrictions, making it suitable for environmental modeling. It is an easy-to-use and efficient tool, especially when data availability is limited. Its architecture enables it to model nonlinear systems with minimal prior knowledge effectively and can combine expert knowledge and empirical data in the form of fuzzy "if-then" rules to construct input-output mappings, thereby providing highly accurate and flexible performance in various applications (Jasmine 2020; Jang 1993; Masroor et al. 2023).

In addition, the ELM model also showed good performance, especially in terms of training speed and generalization ability. Although ELM has a slightly lower accuracy compared to ANFIS, its R^2 value exceeds 0.83 in both datasets, achieving reliable predictions. Its simple architecture and fast computation make it an ideal choice for real-time and large-scale environmental prediction applications.

In contrast, the MARS model has the lowest prediction accuracy, especially on the test dataset ($R^2 = 0.6629$), which indicates that its generalization ability is limited. However, MARS can provide a piecewise linear formulation, thus providing a high interpretability of the model and deep insights into the interactions between variables. However, the model's reliance on a single input variable and a small number of basis functions limits its ability to characterize the complex behavior of rosette jet mixing, resulting in poor prediction results.

In summary, the ANFIS model is the most effective and reliable method among the three models for simulating the normalized concentration field in buoyant rosette jets, followed by ELM and, finally, MARS. This study demonstrates the potential of selecting efficient machine learning models and combining them with experimental techniques for application in computational fluid dynamics, providing a flexible and efficient alternative to traditional methods for scenarios that require fast, accurate, and interpretable predictions.

Chapter IV Conclusion and Recommendations

4.1 Conclusion

Rosette-type multiport diffusers have become an increasingly important component in modern submarine wastewater discharge systems, especially in densely developed coastal regions where spatial constraints and environmental regulations demand compact yet effective designs. By arranging multiple discharge ports in a circular configuration, rosette diffusers enable rapid initial dilution of buoyant effluents—such as municipal wastewater or desalination brine—through enhanced entrainment of ambient seawater. This promotes effective dispersion and helps maintain marine water quality within acceptable ecological thresholds. As a result, rosette diffusers are now widely employed in environmentally sensitive outfall projects worldwide. However, the mixing behavior of rosette buoyant jets is governed by complex flow dynamics, including buoyancy-driven rise, inclined trajectories, and multidirectional jet interactions, which make their prediction far more challenging than that of single or unidirectional jets. Despite the increasing application of rosette jets, the research on its mixing characteristics and prediction models in the literature is still incomplete, which shows the necessity of conducting more systematic research.

This study comprehensively carried out the behavior prediction research on buoyant rosette multiport jets, covering three major methods: experimental observation, numerical simulation and machine learning modeling. By constructing an integrated research framework, laboratory-scale laser induced fluorescence (LIF) experiments and computational fluid dynamics (CFD) simulations were integrated, and the simulation results were systematically compared with the experimental data to evaluate the applicability and accuracy of different turbulence models under various hydraulic conditions. At the same time, a variety of machine learning (ML) models were trained using experimental data to achieve rapid prediction of jet trajectories and normalized concentration fields.

LIF experiments provide high-fidelity concentration fields for model verification and data-driven modeling, while CFD simulations are used to reveal the jet flow structure and performance differences of various turbulence models. By introducing a machine learning model trained based on experimental data, this study further expanded the depth and breadth of buoyant porous jet modeling, provided new ideas and tools for efficient and accurate jet behavior prediction in complex environments and under different operating conditions, and demonstrated good engineering application potential and promotion value.

Experiments using LIF technology have yielded high-resolution scalar concentration fields and visualized jet trajectory data under different operating parameters, which are key reference benchmarks for verifying the accuracy of numerical simulations. CFD simulations were performed using an OpenFOAM solver (pimpleFoam10r) modified from pimpleFoam, which incorporates temperature-driven buoyancy effects while ignoring salinity transport for improved computational efficiency.

Three RANS turbulence models—standard k-ε, RNG k-ε, and SST k-ω—were evaluated. Overall, the RNG k-ε model performs well in predicting centerline trajectories and concentration fields, especially under momentum-dominated conditions, followed by standard k-ε while the lowest performance was demonstrated by the SST k-ω model. Both the standard and RNG k-ε turbulence models contain two transport equations, one for k and the other for ε. Most of the terms in the two closures are the same, but the RNG k-ε model contains some improvements that may help improve the prediction of rosette buoyancy jets. First, the RNG k-ε model considers the effect of the Reynolds number on the effective turbulent transport. Second, the RNG k-ε model uses more advanced equations to determine the inverse effective Prandtl number. Third, the RNG k-ε model includes a new term in ε that can improve the calculation of turbulent viscosity. In addition to model accuracy, another advantage of the RNG k-ε model is that it does not significantly increase the computational cost. Some more advanced turbulence modeling techniques, such as large eddy simulation, detached eddy simulation, and direct numerical simulation techniques, will significantly increase the computational cost and are therefore not considered in this study.

Due to the high computational cost of CFD simulations and the optical limitations of LIF experiments near the nozzle area, this study adopts a data-driven modeling approach based on machine learning (ML) algorithms, using three machine learning models: extreme learning machine (ELM), adaptive neuro-fuzzy inference system (ANFIS), and multivariate adaptive regression spline function (MARS). These models are trained specifically on high-fidelity datasets from LIF experiments that capture the normalized concentration field of buoyant rose-shaped multi-port jets under 34 different Froude number conditions. The input variables include Fr, x/D, and y/D, and the output is the normalized concentration. A total of 870 data points are generated and randomly divided into training and test sets, of which 70% are used for model training and 30% for testing. This division is intended to ensure an objective evaluation of the predictive performance of the machine learning models.

Among the three models, ANFIS has the highest overall accuracy, $R^2 = 0.9088$, MAE = 0.0376 and RMSE = 0.0551 for testing dataset, outperforming ELM and MARS. The ANFIS architecture adopts a five-layer structure that combines fuzzy reasoning with adaptive neural learning, allowing the model to effectively generalize in parameter space while maintaining interpretability through rule-based reasoning. It can accurately capture the nonlinear relationship between flow parameters and concentration field distribution even in areas with local discontinuities or turbulent fluctuations. These advantages make ANFIS particularly suitable for environmental systems where physical uncertainty and data noise are prevalent. The ELM model also achieved good results, especially in terms of computational speed and simplicity. Its single hidden layer structure and analytically derived output weights enable fast training and inference, making it very suitable for large-scale or real-time environmental prediction tasks. Although the extreme learning machine (ELM) is slightly less accurate than the adaptive fuzzy inference system (ANFIS), it maintains strong generalization ability, especially under high concentration conditions. In contrast, the MARS model has the worst prediction performance, especially in the low to medium concentration range. However, the MARS model has high interpretability, gives three basis functions based on a single input variable x_3 (i.e., y/D in this study), adopts a continuous and interpretable piecewise linear structure, and can flexibly capture the nonlinear relationship between input and output. Although the MARS model is interpretable, it has low accuracy and limited generalization ability, making it difficult to accurately predict changes in the concentration field. This may be due to the model's reliance on a single input variable and a limited number of basis functions, which limits its ability to capture multivariate interactions and complex nonlinearities present in the system. Overall, this study demonstrates the potential of selecting efficient machine learning models and combining them with experimental techniques for application in computational fluid dynamics. A reliable framework is provided for simulating complex jet behavior in buoyant rosette diffusers. These models provide comparable accuracy to traditional CFD simulations at significantly reduced computational requirements, thus providing an efficient alternative. This hybrid approach advances the modeling of rosette jet dynamics and provides a flexible and efficient alternative to traditional methods for scenarios that require fast, accurate, and interpretable predictions.

Overall, the hybrid methodology integrating experimental–CFD and experimental–ML approaches presented in this study effectively bridges critical gaps in the modeling of buoyant rosette jets. It enables accurate, efficient, and interpretable simulation of jet dynamics and concentration fields, providing a data-driven solution for optimizing diffuser design and assessing environmental impacts in coastal engineering applications. This integrated framework paves the way for sustainable and intelligent design of wastewater discharge systems under diverse environmental and operational conditions.

4.2 Recommendations for future studies

Based on the outcomes of this study, the following recommendations are proposed:

- Experimental density control improvements： In this study, the density difference was controlled by the temperature contrast between the heated dye solution and the ambient freshwater. However, due to the long transfer path—from the reservoir tank through the constant-head tank and flowmeter to the discharge port—the dye solution experienced cooling before reaching the tank, leading to variations in density difference and, consequently, changes in the Froude number and jet behavior. This introduced some experimental uncertainty. In future studies, more precise density control could be achieved by adding ethanol to the reservoir solution and using a densitometer for direct measurement, thereby ensuring a stable and accurately defined density difference.
- Extension of ML Models: While ANFIS demonstrated excellent accuracy, further enhancements can be achieved by integrating optimization algorithms (e.g., genetic algorithms or particle swarm optimization) for automatic tuning of membership functions and rule structures.
- Real-time Applications: Given their low computational cost, ML models such as ANFIS and ELM are well-suited for real-time control and adaptive management of outfall systems. Future work should explore the deployment of trained models in operational settings.
- Inclusion of Additional Physical Parameters: Expanding the training datasets to include more diverse hydraulic and ambient conditions (e.g., crossflow, stratification, unsteady inputs) could improve model robustness and extend applicability to broader environmental scenarios.

References

Aredah, A. S., Ertugrul, O. F., Sattar, A. A., Bonakdari, H., & Gharabaghi, B. (2022). Extreme

Learning Machine model for assessment of stream health using the Qualitative Habitat Evaluation Index. *Water Science & Technology. Water Supply*, *22*(5), 5355–5375. https://doi.org/10.2166/ws.2022.166

Azimi, H., Bonakdari, H., & Ebtehaj, I. (2017a). Sensitivity analysis of the factors affecting the discharge capacity of side weirs in trapezoidal channels using extreme learning machines. *Flow Measurement and Instrumentation*, *54*, 216–223. https://doi.org/10.1016/j.flowmeasinst.2017.02.005

Azimi, H., Bonakdari, H., Ebtehaj, I., Ashraf Talesh, S. H., Michelson, D. G., & Jamali, A. (2017b). Evolutionary Pareto optimization of an ANFIS network for modeling scour at pile groups in clear water condition. *Fuzzy Sets and Systems*, *319*, 50–69. https://doi.org/10.1016/j.fss.2016.10.010

Azimi, H., Bonakdari, H., Ebtehaj, I., & Michelson, D. G. (2018). A combined adaptive neuro-fuzzy inference system–firefly algorithm model for predicting the roller length of a hydraulic jump on a rough channel bed. *Neural Computing & Applications*, *29*(6), 249–258. https://doi.org/10.1007/s00521-016-2560-9

Bonakdari, H., Gholami, A., Gharabaghi, B., Ebtehaj, I., Akhtari, A. A., & Arai, K. (2021). An Assessment of Extreme Learning Machine Model for Estimation of Flow Variables in Curved Irrigation Channels. In *Intelligent Computing* (Vol. 285, pp. 259–269). Springer International Publishing AG. https://doi.org/10.1007/978-3-030-80129-8_19

Bonakdari, H., Qasem, S. N., Ebtehaj, I., Zaji, A. H., Gharabaghi, B., & Moazamnia, M. (2020). An expert system for predicting the velocity field in narrow open channel flows using self-adaptive extreme learning machines. *Measurement: Journal of the International Measurement Confederation*, *151*, 107202-. https://doi.org/10.1016/j.measurement.2019.107202

Brunton, S. L., Noack, B. R., & Koumoutsakos, P. (2020). Machine Learning for Fluid Mechanics. *Annual Review of Fluid Mechanics*, *52*(1), 477–508. https://doi.org/10.1146/annurev-fluid-010719-060214

Cheung, S. K. B., Leung, D. Y. L., Wang, W., Lee, J. H. W., & Cheung, V. (2000). VISJET-a computer ocean outfall modelling system. *Proceedings Computer Graphics International 2000*, 75–80. https://doi.org/10.1109/CGI.2000.852322

Duraisamy, K., Iaccarino, G., & Xiao, H. (2019). Turbulence Modeling in the Age of Data. *Annual Review of Fluid Mechanics*, *51*(1), 357–377. https://doi.org/10.1146/annurev-fluid-010518-040547

Ebtehaj, I., Bonakdari, H., Moradi, F., Gharabaghi, B., & Khozani, Z. S. (2018). An integrated framework of Extreme Learning Machines for predicting scour at pile groups in clear water condition. Coastal Engineering (Amsterdam), 135, 1–15. https://doi.org/10.1016/j.coastaleng.2017.12.012

Ebtehaj, I., Bonakdari, H., & Shamshirband, S. (2016). Extreme learning machine assessment for estimating sediment transport in open channels. *Engineering with Computers*, *32*(4), 691–704. https://doi.org/10.1007/s00366-016-0446-1

Ebtehaj, I., Bonakdari, H., Zaji, A. H., & Sharafi, H. (2019). Sensitivity analysis of parameters affecting scour depth around bridge piers based on the non-tuned, rapid extreme learning machine method. *Neural Computing & Applications*, *31*(12), 9145–9156. https://doi.org/10.1007/s00521-018-3696-6

Elmisaoui, S., Kissami, I., Ghidaglia, J.-M., Ezziyyani, M., Kacprzyk, J., & Balas, V. E. (2024). High-Performance Computing to Accelerate Large-Scale Computational Fluid Dynamics Simulations: A Comprehensive Study. In *International Conference on Advanced Intelligent Systems for Sustainable Development (AI2SD'2023)* (pp. 352–360). Springer Nature Switzerland. https://doi.org/10.1007/978-3-031-54318-0_31

Fischer, H. B. (1979). *Mixing in inland and coastal waters*. Academic Press

Forrester, A. I. J., Sóbester, A., & Keane, A. J. (2008). *Engineering design via surrogate modelling: a practical guide*. J. Wiley.

Friedman, J. H. (1991). Multivariate Adaptive Regression Splines. *The Annals of Statistics*, *19*(1), 1–67. https://doi.org/10.1214/aos/1176347963

Gholami, A., Bonakdari, H., Ebtehaj, I., Mohammadian, M., Gharabaghi, B., & Khodashenas, S.

R. (2018). Uncertainty analysis of intelligent model of hybrid genetic algorithm and particle swarm optimization with ANFIS to predict threshold bank profile shape based on digital laser approach sensing. *Measurement: Journal of the International Measurement Confederation*, *121*, 294–303. https://doi.org/10.1016/j.measurement.2018.02.070

Huai, W., Li, Z., Qian, Z., Zeng, Y., Han, J., & Peng, W. (2010). Numerical simulation of horizontal buoyant wall jet. *Journal of Hydrodynamics. Series B*, *22*(1), 58–65. https://doi.org/10.1016/S1001-6058(09)60028-7

Huang, G.-B., Zhu, Q.-Y., & Siew, C.-K. (2006). Extreme learning machine: Theory and applications. *Neurocomputing (Amsterdam), 70(1), 489–501.* https://doi.org/10.1016/j.neucom.2005.12.126

Huang, G., Huang, G.-B., Song, S., & You, K. (2015). Trends in extreme learning machines: A review. *Neural Networks*, *61*, 32–48. https://doi.org/10.1016/j.neunet.2014.10.001

Isaacson, M. S., Koh, R. C. Y., & Brooks, N. H. (1983). Plume Dilution for Diffusers with Multiport Risers. *Journal of Hydraulic Engineering (New York, N.Y.)*, *109*(2), 199–220. https://doi.org/10.1061/(ASCE)0733-9429(1983)109:2(199)

Issa, R. I. (1986). Solution of the implicitly discretised fluid flow equations by operator-splitting. *Journal of Computational Physics*, *62*(1), 40–65.https://doi.org/10.1016/0021-9991(86)90099-9

Jamshed, S. (2015). *Using HPC for computational fluid dynamics: a guide to high performance computing for CFD engineers* (1st edition). Academic Press.

Jang, J.-S. R. (1993). ANFIS: adaptive-network-based fuzzy inference system. *IEEE Transactions on Systems, Man, and Cybernetics*, *23*(3), 665–685.https://doi.org/10.1109/21.256541

Jasmine, M., Mohammadian, A., Bonakdari, H., & University of Ottawa. Department of Civil Engineering. (2020). *A Comparative Study on Prediction of Evaporation in Arid Area Based on Artificial Intelligence Techniques*. Université d'Ottawa / University of Ottawa.

Jirka, G. H. (1977). Discussion: "An Analysis of Deep Submerged Multiple-Port Buoyant Discharges" (Kannberg, L. D., and Davis, L. R., 1979, ASME J. Heat Transfer, 99, pp. 648–654). *Journal of Heat Transfer*, *99*(4), 654–654. https://doi.org/10.1115/1.3450758

Jirka, G. H. (2004). Integral model for turbulent buoyant jets in unbounded stratified flows. Part I: Single round jet. *Environmental Fluid Mechanics (Dordrecht, Netherlands: 2001)*, *4*(1), 1–56. https://doi.org/10.1023/A:1025583110842

Kheirkhah Gildeh, H., & University of Ottawa. Department of Civil Engineering. (2013). *Numerical Modeling of Thermal/Saline Discharges in Coastal Waters*. Thesis (M.A.Sc.)--University of Ottawa, 2013.

Khuntia, J. R., Devi, K., Sahoo, S., Das, B. S., & Khatua, K. K. (2023). CFD Simulation of Non-prismatic Compound Channels Using k–ε and k–ω Turbulence Models. In *International Conference on Hydraulics, Water Resources and Coastal Engineering* (pp. 19-49). Singapore: Springer Nature Singapore. https://doi.org/10.1007/978-981-97-8035-8_2

Kwon, S. J., & Seo, I. W. (2005). Experimental Investigation of Wastewater Discharges from a Rosette-type Riser Using PIV. *KSCE Journal of Civil Engineering*, *9*(5), 355–362. https://doi.org/10.1007/BF02830626

Lai, A. C. H., Yu, D., & Lee, J. H. W. (2011). Mixing of a Rosette Jet Group in a Crossflow. *Journal of Hydraulic Engineering (New York, N.Y.)*, *137*(8), 787–803. https://doi.org/10.1061/(ASCE)HY.1943-7900.0000359

Lai, C. C. K., & Lee, J. H. W. (2012). Mixing of inclined dense jets in stationary ambient. *Journal of Hydro-Environment Research*, *6*(1), 9–28. https://doi.org/10.1016/j.jher.2011.08.003

Launder, B. E., & Spalding, D. B. (1972). *Lectures in mathematical models of turbulence*. Academic Press.

Masroor, M., Razavi-Termeh, S. V., Rahaman, M. H., Choudhari, P., Kulimushi, L. C., & Sajjad, H. (2023). Adaptive neuro fuzzy inference system (ANFIS) machine learning algorithm for assessing environmental and socio-economic vulnerability to drought: a study in Godavari middle sub-basin, India. *Stochastic Environmental Research and Risk Assessment*, *37*(1), 233–259. https://doi.org/10.1007/s00477-022-02292-1

Menter, F. R. (1994). Two-equation eddy-viscosity turbulence models for engineering applications. *AIAA Journal*, *32*(8), 1598–1605. https://doi.org/10.2514/3.12149

Merabet, K., & Heddam, S. (2023). Improving the accuracy of air relative humidity prediction using hybrid machine learning based on empirical mode decomposition: a comparative study. *Environmental Science and Pollution Research International*, *30*(21), 60868–60889. https://doi.org/10.1007/s11356-023-26779-8

Millero, F. J., & Poisson, A. (1981). International one-atmosphere equation of state of seawater. *Deep-Sea Research. Part A. Oceanographic Research Papers*, *28*(6), 625–629. https://doi.org/10.1016/0198-0149(81)90122-9

Moukalled, F., Darwish, M., Kasamani, J., Hammoud, A., & Mansour, M. K. (2016). Buoyancy-induced flow and heat transfer in a porous annulus between concentric horizontal circular and square cylinders. *Numerical Heat Transfer. Part A, Applications*, *69*(9), 1029–1050. https://doi.org/10.1080/10407782.2015.1090847

Nayeem, A., Bonakdari, H., Khalloufi, S., & Aider, M. (2025). Application of multivariate adaptive regression splines (MARS) to study the colorization occurring in the process of lactulose production following lactose electro-activation. *International Dairy Journal*, 106291. https://doi.org/10.1016/j.idairyj.2025.106291

Puggioni, L., Boga, G., Cimarelli, A., Crialesi Esposito, M., Musacchio, S., Stalio, E., & Boffetta, G. (2025). Transition to the buoyancy-dominated regime in a planar temporal forced plume. *Journal of Fluid Mechanics*, *1002*. https://doi.org/10.1017/jfm.2024.1237

Roberts, P. J. W. (1979). Line plume and ocean outfall dispersion. *Journal of the Hydraulics Division*, *105*(4), 313-331. https://doi.org/10.1061/JYCEAJ.0005175

Roberts, P. J. W., & Snyder, W. H. (1993a). Hydraulic Model Study for Boston Outfall. I: Riser Configuration. *Journal of Hydraulic Engineering (New York, N.Y.)*, *119*(9), 970–987. https://doi.org/10.1061/(ASCE)0733-9429(1993)119:9(970)

Roberts, P. J. W., & Snyder, W. H. (1993b). Hydraulic Model Study for Boston Outfall. II: Environmental Performance. *Journal of Hydraulic Engineering (New York, N.Y.)*, *119*(9), 988–1002. https://doi.org/10.1061/(ASCE)0733-9429(1993)119:9(988)

Roberts, P. J., Salas, H. J., Reiff, F. M., Libhaber, M., Labbe, A., & Thomson, J. C. (2010). *Marine wastewater outfalls and treatment systems*. IWA publishing. https://doi.org/10.2166/9781780401669

Roohi, E., Pendar, M.-R., & Rahimi, A. (2016). Simulation of three-dimensional cavitation behind a disk using various turbulence and mass transfer models. *Applied Mathematical Modelling*, *40*(1), 542–564. https://doi.org/10.1016/j.apm.2015.06.002

Saeidi Hosseini, S. A. R., Mohammadian, A., Roberts, P. J. W., & Abessi, O. (2022). Numerical Study on the Effect of Port Orientation on Multiple Inclined Dense Jets. *Journal of Marine Science and Engineering*, *10*(5), 590-. https://doi.org/10.3390/jmse10050590

Seo, I. W., & Yeo, H. K. (2002). Near-field dilution of rosette type multiport wastewater diffusers. *Water engineering research: international journal of KWRA*, *3*(2), 93-111. https://doi.org/10.1061/(ASCE)HY.1943-7900.0000409

Seo, I. W., Kwon, S. J., & Yeo, H. K. (2004). Merging Characteristics of Buoyant Discharges from Rosette-Type Diffusers in Shallow Water. *KSCE Journal of Civil Engineering*, *8*(6), 679–688. https://doi.org/10.1007/BF02823559

Shaghaghi, S., Bonakdari, H., Gholami, A., Kisi, O., Binns, A., & Gharabaghi, B. (2019). Predicting the geometry of regime rivers using M5 model tree, multivariate adaptive regression splines and least square support vector regression methods. *International Journal of River Basin Management*, *17*(3), 333–352. https://doi.org/10.1080/15715124.2018.1546731

Tahmooresi, S., Goodarzi, D., Mohammadian, A., & Nistor, I. (2025). LIF measurement of turbulent horizontal dense jets in stagnant ambient. *International Journal of Heat and Mass Transfer*, *244*, 126867-. https://doi.org/10.1016/j.ijheatmasstransfer.2025.126867

Tao, H., Al-Khafaji, Z. S., Qi, C., Zounemat-Kermani, M., Kisi, O., Tiyasha, T., Chau, K.-W., Nourani, V., Melesse, A. M., Elhakeem, M., Farooque, A. A., Pouyan Nejadhashemi, A., Khedher, K. M., Alawi, O. A., Deo, R. C., Shahid, S., Singh, V. P., & Yaseen, Z. M. (2021). Artificial intelligence models for suspended river sediment prediction: state-of-the art, modeling framework appraisal, and proposed future research directions. *Engineering Applications of Computational Fluid Mechanics*, *15*(1), 1585–1612. https://doi.org/10.1080/19942060.2021.1984992

Tate, P. M. (2002). *The rise and dilution of buoyant jets and their behaviour in an internal wave field* (Doctoral dissertation, UNSW Sydney).

Tian, X., & Roberts, P. J. W. (2011). Experiments on Marine Wastewater Diffusers with Multiport Rosettes. *Journal of Hydraulic Engineering (New York, N.Y.)*, *137*(10), 1148–1159. https://doi.org/10.1061/(ASCE)HY.1943-7900.0000409

Tuković, Ž., & Jasak, H. (2012). A moving mesh finite volume interface tracking method for surface tension dominated interfacial fluid flow. *Computers & Fluids*, *55*, 70–84. https://doi.org/10.1016/j.compfluid.2011.11.003

Wang, X., Mohammadian, A., & University of Ottawa. Department of Civil Engineering. (2020). *Numerical Modeling of Inclined Dense Jets in Stagnant Water on a Sloped Bottom*. Université d'Ottawa / University of Ottawa.

Weller, H. G., Tabor, G., Jasak, H., & Fureby, C. (1998). A tensorial approach to computational continuum mechanics using object-oriented techniques. *Computers in Physics*, *12*(6), 620–631. https://doi.org/10.1063/1.168744

Wu, J. Y., Lv, R. R., Huang, Y. Y., & Yang, G. (2021). Flow Structure Transition and Hysteresis of Turbulent Mixed Convection Induced by a Transverse Buoyant Jet. *International Journal of Heat and Mass Transfer*, *177*, 121310-. https://doi.org/10.1016/j.ijheatmasstransfer.2021.121310

Yakhot, V., & Orszag, S. A. (1986). Renormalization-Group Analysis of Turbulence. *Physical Review Letters*, *57*(14), 1722–1724. https://doi.org/10.1103/PhysRevLett.57.1722

Yan, X., & Mohammadian, A. (2017). Numerical Modeling of Vertical Buoyant Jets Subjected to Lateral Confinement. *Journal of Hydraulic Engineering (New York, N.Y.)*, *143*(7). https://doi.org/10.1061/(ASCE)HY.1943-7900.0001307

Yan, X., Mohammadian, A., & Chen, X. (2019). Three-Dimensional Numerical Simulations of Buoyant Jets Discharged from a Rosette-Type Multiport Diffuser. *Journal of Marine Science and Engineering*, *7*(11), 409-. https://doi.org/10.3390/jmse7110409

Yan, X., & Mohammadian, A. (2019). Numerical Modeling of Multiple Inclined Dense Jets Discharged from Moderately Spaced Ports. *Water (Basel)*, *11*(10), 2077-. https://doi.org/10.3390/w11102077

Yan, X., & Mohammadian, A. (2020). Prediction of a rosette dense jet group in crossflow ambient conditions using multi-gene genetic programming. *Desalination and Water Treatment*, *190*, 440–448. https://doi.org/10.5004/dwt.2020.25746

Yan, X., Wang, Y., Mohammadian, A., & Liu, J. (2021). Simulations of the Concentration Fields of Rosette-Type Multiport Buoyant Discharges Using Combined CFD and Multigene Genetic Programming Techniques. *Journal of Marine Science and Engineering*, *9*(11), 1311-. https://doi.org/10.3390/jmse9111311

Yan, X., Wang, Y., Mohammadian, A., Liu, J., & Chen, X. (2022). CFD-CNN Modeling of the Concentration Field of Multiport Buoyant Jets. *Journal of Marine Science and Engineering*, *10*(10), 1383-. https://doi.org/10.3390/jmse10101383